Thermal tides on Mars before and during the 2018 Global Dust Event as observed by TIRVIM-ACS onboard ExoMars Trace Gas Orbiter

Sandrine Guerlet, S Fan, François Forget, N Ignatiev, Ehouarn Millour, A Kleinböhl, A Shakun, A Grigoriev, A Trokhimovskiy, Franck Montmessin, et al.

JGR Planets

RESEARCH ARTICLE
10.1029/2023JE007851

Thermal Tides on Mars Before and During the 2018 Global Dust Event as Observed by TIRVIM-ACS Onboard ExoMars Trace Gas Orbiter

S. Guerlet[1,2], S. Fan[1], F. Forget[1], N. Ignatiev[3], E. Millour[1], A. Kleinböhl[4], A. Shakun[3], A. Grigoriev[5], A. Trokhimovskiy[3], F. Montmessin[6], and O. Korablev[3]

[1]LMD/IPSL, Sorbonne Université, PSL Research University, École Normale Supérieure, École Polytechnique, CNRS, Paris, France, [2]LESIA, Observatoire de Paris, CNRS, Sorbonne Université, Université Paris-Diderot, Meudon, France, [3]Space Research Institute (IKI), Moscow, Russia, [4]Jet Propulsion Laboratory, California Institute of Technology, Pasadena, CA, USA, [5]Research School of Astronomy and Astrophysics, Australian National University, Canberra, ACT, Australia, [6]LATMOS/IPSL, Guyancourt, France

Abstract Migrating tides dominate the tropical climate on Mars and are known to reach high amplitudes during global dust events (GDE). In this study, we characterize the amplitude, phase and vertical wavelength of the diurnal and semidiurnal migrating tides in Mars' lower atmosphere (up to 50 km) by exploiting temperature vertical profiles retrieved from TIRVIM, an infrared spectrometer onboard the ExoMars Trace Gas Orbiter covering multiple local times. Observations from the Mars Climate Sounder onboard the Mars Reconnaissance Orbiter are used to complement the local time coverage when needed, and to estimate a seasonal trend to subtract from TIRVIM observations. We focus on two time periods in Martian Year 34, near Ls = 150° and near Ls = 200° (during the 2018 GDE). The characteristics of the migrating tides at Ls = 150° agree very well with tidal theory: a downward propagation, amplitudes of typically 2–5 K, and a larger vertical wavelength for the semidiurnal compared to the diurnal mode. Comparisons with model predictions from the Mars Planetary Climate Model reveal an excellent agreement, except for a slightly different phase of the diurnal tide. During the GDE, the tide pattern changes spectacularly: the diurnal tide amplitude reaches 35 K at 65°S and 17 K at 50°N, being vertically trapped up to 10 Pa. The semidiurnal tide is maximum near 20–30°S with an amplitude of 8–12 K. The phase of this mode is tilted with latitude, which was not the case before the storm. This indicates a significant contribution of the asymmetric Hough modes due to hemispheric asymmetry in the dust distribution.

Plain Language Summary Important temperature variations are observed in the Martian atmosphere at diurnal scale. Part of these variations are due to a phenomenon called migrating thermal tides, which take the form of global oscillations with periods that are diurnal, or fractions of a day (half a day period = semidiurnal, a third of a day = terdiurnal, etc). Using satellite observations sampling different local times on Mars, we separated these different components and derived their amplitude and phase (the local time at which these oscillations peak) in particular during the global dust event that occurred in 2018. During this major storm, diurnal temperature variations reached 65 K at high southern latitudes near 25 km altitude between the late morning (minimum of temperature) and late evening (maximum of temperature). We also report on the characteristics of the semidiurnal tide and even the terdiurnal tide, which have been less studied during dust storms. The phase of the semidiurnal tide is not the same at all latitudes, which we interpret as a consequence of the asymmetric dust distribution (more dust in the southern hemisphere). Our results agree with predictions from a Global Climate Model, although some small disagreements are found, calling for future improvements in the model.

Key Points:

- The characteristics of the migrating tides derived from TIRVIM at Ls = 150° agree with tidal theory and model predictions
- During the 2018 global dust event (GDE), the diurnal tide reached an amplitude of 35 K at 65°S and we tentatively detect the terdiurnal tide
- During the 2018 GDE, the semidiurnal tide amplitude reached 10 K at 20°S and exhibited a phase tilt with latitude

Correspondence to:
S. Guerlet,
sandrine.guerlet@lmd.jussieu.fr

Citation:
Guerlet, S., Fan, S., Forget, F., Ignatiev, N., Millour, E., Kleinböhl, A., et al. (2023). Thermal tides on Mars before and during the 2018 global dust event as observed by TIRVIM-ACS onboard ExoMars Trace Gas Orbiter. *Journal of Geophysical Research: Planets*, *128*, e2023JE007851. https://doi.org/10.1029/2023JE007851

Received 6 APR 2023
Accepted 10 AUG 2023

Author Contributions:
Formal analysis: S. Guerlet
Investigation: S. Guerlet, S. Fan, F. Forget, E. Millour
Methodology: S. Guerlet, N. Ignatiev, A. Shakun, A. Grigoriev, A. Trokhimovskiy
Project Administration: O. Korablev
Validation: A. Kleinböhl
Writing – original draft: S. Guerlet
Writing – review & editing: S. Guerlet, S. Fan, F. Forget, N. Ignatiev, E. Millour, A. Kleinböhl, F. Montmessin

1. Introduction

Thermal tides are the dynamical response of the atmosphere to diurnal solar heating. While they have a small amplitude on Earth, they dominate the tropical climate on Mars, due to its much smaller atmospheric density. Tides are sorted in different categories according to their direction of propagation (eastward or westward), their zonal wavenumber s and period per sol σ. Among them, migrating thermal tides are Sun-synchronous, hence propagate westward with the Sun, with periods that are integer fractions of the solar day. The main harmonics are the diurnal migrating tide (with a diurnal period and a zonal wavenumber of one, i.e., $s = \sigma = 1$), referred to as

DW1, followed by the semidiurnal migrating tide ($s = \sigma = 2$) SW2 and the terdiurnal tide ($s = \sigma = 3$) TW3 (Forbes et al., 2020). The meridional and vertical structures of such tides are expected to be a combination of Hough functions, as predicted from classical tide theory (Lindzen, 1970; Wilson & Hamilton, 1996; Zurek, 1976). A given harmonic response (DW1, SW2, …) can be decomposed in several modes (through the Hough functions), some of which propagate vertically while others are vertically trapped. As they are thermally forced, tide amplitudes are expected to vary depending on dust and water ice cloud content (e.g., Wilson & Richardson, 2000). In particular, a spectacular increase of the amplitude of the DW1 tide at extratropical latitudes have been reported during global dust events (GDEs) (e.g., Guzewich et al., 2014) and the amplitude of the SW2 harmonics was found to be linked to the radiative effect of water ice clouds (Kleinböhl et al., 2013) and vertically extending dust forcing (Steele et al., 2021; Wilson & Hamilton, 1996).

These modes have been previously studied by a variety of instruments, from surface pressure sensors (where the SW2 signature is particularly clean, e.g., Leovy & Zurek, 1979) to upper atmospheric density measurements (e.g., Lo et al., 2015). In this paper we focus on tide signatures measured in the tropospheric temperature fields derived from TIRVIM (Thermal InfraRed channel in honor of professor Vassilii Ivanovich Moroz), the thermal infrared spectrometer of the Atmospheric Chemistry Suite (ACS) instrument onboard the Trace Gas Orbiter (TGO) spacecraft (Guerlet et al., 2022; Korablev et al., 2018). Similar past investigations were mostly based on instruments mounted on Sun-synchronous orbiters such as the Thermal Emission Spectrometer (TES) onboard the Mars Global Surveyor (Banfield et al., 2000; Guzewich et al., 2014) and the Mars Climate Sounder (MCS) onboard the Mars Reconnaissance Orbiter (Lee et al., 2009). The identification and characterization of the thermal tides from these data sets is inherently hampered by their limited local time coverage (near 2–3 a.m. and 2–3 p.m.). Combining in-track and cross-track MCS limb observations (which provides observations at six different local times) allowed Kleinböhl et al. (2013) and Wu et al. (2015) to partially address the aliasing issues and derive the amplitude of the semidiurnal migrating tides and several non-migrating tides. However, unequal spacing in local time of the six observations leads to very large uncertainties: Kleinböhl et al. (2013) report uncertainties of 4–5 K on the derived SW2 amplitude.

More recently, two other thermal infrared spectrometers onboard non-Sun synchronous orbiters have allowed to even more precisely derive the tide amplitudes and phases, namely from TIRVIM/TGO (Fan, Guerlet, et al., 2022) and EMIRS onboard the Emirates Mars Mission (Fan, Forget, et al., 2022). Both studies focused on evaluating migrating tide properties at Ls = 90° during Martian Year 35 (for the TIRVIM study) and 36 (for the EMIRS study). The nearly complete local time coverage of these two instruments yielded unprecedented estimates of the phases of the tides, although it was found that in the case of TIRVIM, aliasing between seasonal and local time sampling (TIRVIM covers the full diurnal cycle over a Martian month) impacted the determination of semidiurnal tide properties. On the other hand, EMM can monitor all local times over ∼10 sols, which allowed the authors to identify and characterize for the first time the terdiurnal mode in such thermal infrared observations. In both studies, a good agreement was found with model predictions except for a ∼2-hr shift in the phase of the diurnal mode. Continuing to monitor and document the tides characteristics at other seasons is important to better understand their forcing mechanisms and their link with the global circulation. In particular, extreme changes in the tide characteristics are expected during dust storms. TIRVIM witnessed a GDE in 2018 during MY34 that has been already studied from the MCS point of view but only at two local times. Indeed, Kleinböhl et al. (2020) reported a strong increase in diurnal tide amplitude, reaching 29 K at 60°S, but the authors could not study other tide modes. On the other hand, Vlasov et al. (2022) studied the global thermal structure of the Martian atmosphere during the MY34 GDE from TIRVIM observations, but not specifically the tide characteristics.

In this paper, we complete these existing studies by constraining the amplitudes and phases of the diurnal and semidiurnal thermal tides from ACS/TIRVIM data acquired at other seasons: we report on the tide characteristics observed in April–May 2018, near Ls = 150° of MY34, and then in June–July 2018, during the global dust event (GDE) of that year, around Ls = 200°. Compared to Fan, Guerlet, et al. (2022), we hereby attempt to quantify and remove the seasonal variability component of TIRVIM observations by using concomitant MCS ones. These observations, along with our methodology of tide decomposition and seasonal de-trending, are described in Section 2. Results on tide characteristics are then detailed and discussed in Section 3 for the pre-storm conditions, and in Section 4 for the MY34 global dust event. Comparisons with predictions from the Mars Planetary Climate Model (PCM) are included in both these sections. Finally, we summarize our results and conclude in Section 5.

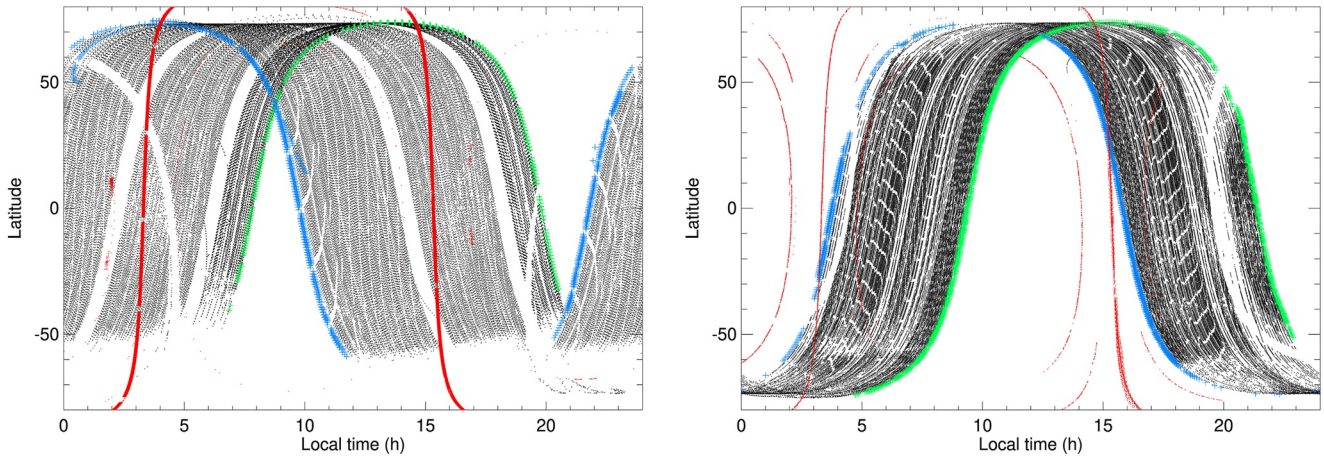

Figure 1. Latitude-local time coverage of individual TIRVIM observations, shown as black dots between Ls = 142° and 167° (March 13 to 28 April 2018, left panel) and between Ls = 197° and 212° during the global dust event of MY34 (21 June till 15 July 2018, right panel). To give a sense of how time (Ls) flows, the first and last orbits are colored in green and blue, respectively. Red dots show the coverage of Mars Climate Sounder data for the same time periods: most of them are "along-track" data, centered near 3 a.m. and 3 p.m.

2. Observations and Method

2.1. TIRVIM Observations

TIRVIM is a Fourier-transform spectrometer, part of the Atmospheric Chemistry Suite (ACS, Korablev et al., 2018). It is mounted on board the ExoMars TGO, an ESA-Roscosmos satellite whose scientific campaign began in March, 2018. While TGO is still operational, TIRVIM cryocooler stopped functioning in December, 2019. TIRVIM mostly operated in nadir geometry, where it recorded thermal emission of Mars' surface and atmosphere with sufficient signal-to-noise ratio between 600 and 1,300 cm^{-1} and with a spectral resolution of 1.2 cm^{-1}. TGO lies on a near circular orbit at 400-km altitude with an inclination of 74°. Its orbit design is such that the local time of TIRVIM nadir observations drifted by 13 min earlier each sol. After 54 sols, a full coverage of the daily cycle was achieved. We have developed an algorithm based on optimal estimation theory to simultaneously retrieve, from TIRVIM nadir spectra, the surface temperature, the vertical profiles of the temperature between a few km and 50–55 km (2–3 Pa), and the column optical depth of dust and water ice clouds (Guerlet et al., 2022). The retrieved temperature profiles have a vertical resolution of typically 10 km (or one atmospheric scale height) in the lower atmosphere and an even coarser resolution of 20 km in the range 2–20 Pa. Details of our algorithm along with a cross-validation exercise of the retrieved temperature profiles with those acquired by the MCS can be found in Guerlet et al. (2022).

In this paper we consider vertical temperature profiles retrieved from TIRVIM data acquired over two periods of Northern Hemisphere summer and autumn of MY34. The first set corresponds to the first 45 sols of its operations, between March 13 and 28 April 2018, that is, from Ls = 142° till Ls = 167° of MY34. An issue with the stability controller of the double pendulum movement was encountered on April 28 (and lasted over a month), which is the reason for stopping our first selection at this date. Figure 1 (left panel) shows the coverage of these observations as a function of latitude and local time. Over these 45 sols, almost a full coverage of the daily cycle was obtained. Only local times between 7 and 10 a.m. are missing south of 20°N, and local times between 7 and 10 p.m. are missing north of 20°S. Latitudes south of 55°S are mostly missing at all local times: spectra were of poor-quality in this area, due to cold surface temperatures (hence low signal and signal-to-noise ratio).

The second set was acquired during the global dust event of MY34. Initially, a dust storm started locally on 2 June 2018 (Ls = 186°) near the equator, then moved southward along Acidalia dust storm track and extended both northward and southward. This dust event reached a mature phase and became planet-encircling from 21 June (Ls = 197°) onward (Kass et al., 2020), which is thus chosen as the starting date of our selection of TIRVIM data. On 15 July (Ls = 212°), an overheating event of TIRVIM detectors occurred and the instrument had to be turned off for several weeks. Hence, 25 sols of TIRVIM observations are available during the peak of the global dust event, covering local times 3:30–9:30 a.m. and 3:30–9:30 p.m. (for equatorial observations). The corresponding latitude versus local time coverage is shown in Figure 1.

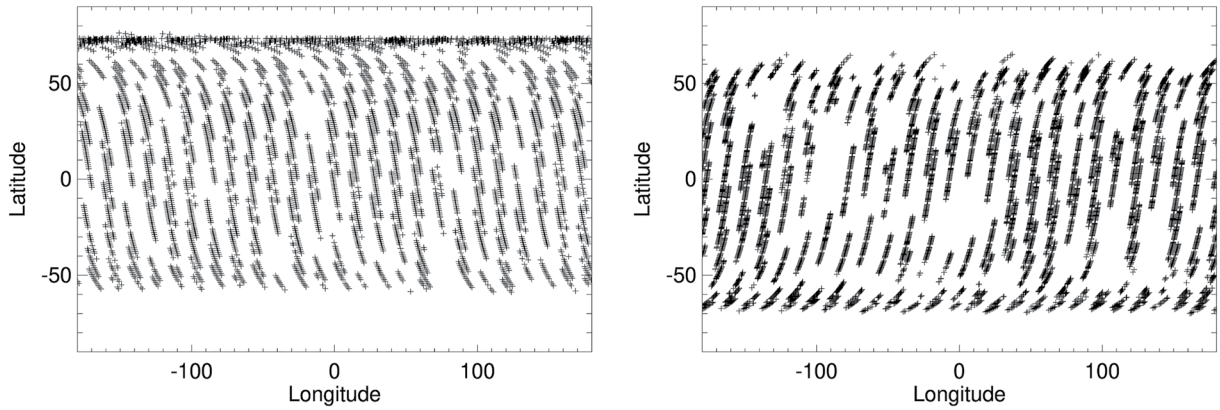

Figure 2. Longitude–latitude coverage of individual TIRVIM observations within a given 45-min long bin in local time. Left: for the bin 11:15 a.m.–12:00 a.m., Ls between 142 and 167°; Right: for the bin 5:15 a.m.–6:00 a.m., Ls between 197 and 212°.

2.2. Decomposition of Thermal Tide Modes

Our aim is to constrain the migrating tide amplitudes and phases by exploiting the retrieved temperature profiles acquired at various local times by TIRVIM. Zonal variations seen in a fixed local time reference frame can be the signature of stationary waves or non-migrating tides. On the other hand, migrating tides are by definition zonally symmetric in a fixed local time reference frame ($m = s - \sigma = 0$). In the following we thus exploit the zonally averaged temperature, where stationary waves and non-migrating tides should be averaged out so that we are left only with the zonally symmetric component of thermal tides (the $m = 0$ modes). This approach has been used in a large number of studies since the Viking epoch, and is similar to that used for instance by Kleinböhl et al. (2013).

We proceed by binning these profiles in bins 45 min-long in local time, 5 or 10°-wide in latitude (see below), and 20°-wide in longitude. Examples of the latitude–longitude coverage for a given 45-min bin is shown in Figure 2. Our nominal choice for the latitudinal bin width is 10°, which ensures a high enough number of observations within the bin (at least 10). We switch to a 5°-wide bin in regions of strong latitudinal temperature gradients, near the polar vortex, to limit the effect of mixing temperature variations of different nature (both diurnal and meridional) if the latitudinal sampling is not uniform among different local time bins. We then take the zonal average of each (latitude, local time, pressure) bin. We retain only the bins with sufficient longitudinal coverage, that is, with at least 15 out of 18 longitudinal bins filled with temperature data.

For each latitude bin and pressure level, we assume that the local time variations of the zonally averaged temperature can be split into three components: a daily average temperature T_{avg} plus the modulations due to the DW1 and SW2 harmonics of the migrating thermal tides. During the GDE, we tested adding two other parameters to fit the terdiurnal TW3 component, as justified in Section 4.2.1. We thus fit the following function to the observations:

$$T(t,\lambda,p) = T_{\text{avg}}(\lambda,p) + A_1(\lambda,p)\cos(t-\phi_1(\lambda,p)) + A_2(\lambda,p)\cos(2t-2\phi_2(\lambda,p)) + A_3(\lambda,p)\cos(3t-3\phi_3(\lambda,p)) \quad \text{(only for the GDE case)} \tag{1}$$

with $T(t, \lambda, p)$ the temperature at a given latitude λ, pressure level p and local time t; A_1, A_2, and A_3 the amplitudes of the diurnal, semidiurnal and terdiurnal modes, and ϕ_1, ϕ_2, and ϕ_3 their phases. The quality of the fit to TIRVIM temperatures is assessed by computing a χ^2 value:

$$\chi^2(\lambda,p) = \sum_t \left(\frac{(T_{\text{TIRVIM}}(t,\lambda,p) - T(t,\lambda,p))}{\sigma(t,\lambda,p)} \right)^2 \tag{2}$$

with σ the standard deviation of uncertainty on the zonally averaged retrieved temperatures, defined in Section 3.4. Using Equation 1 to fit the observations assumes that all the variability seen in the binned data at a given latitude and pressure level can be attributed to diurnal variations. However, as the local time sampling of TIRVIM data drifts with time (see Figure 1), our data set actually displays a combination of diurnal and seasonal or synoptic variations. If there are significant seasonal changes over a few tens of sols (a typical time interval needed to cover multiple local times with TIRVIM), the risk is then to wrongly interpret those seasonal or synoptic changes as

local time variations. As discussed in Fan, Guerlet, et al. (2022), this could significantly impact the derived amplitude of the semidiurnal tides from TIRVIM, due to the specifics of TGO's orbit. Indeed, in the scenario where the temperature would regularly increase between Ls = 142° and 167°, then from TIRVIM point of view, this would be seen as two trends of temperature increasing toward earlier local times, one from 7 p.m. to 10 a.m. and the other from 7 a.m. to 10 p.m. (we recall that the instrument samples the atmosphere at two local times 12 hr apart for each 2-hr long TGO orbit, see Figure 1), creating a "false" semidiurnal tide signature. We present a way to mitigate this effect in the next subsection.

2.3. Seasonal De-Trending From Mars Climate Sounder Data

To estimate the magnitude of seasonal changes over the course of the TIRVIM time series considered here, we exploit temperature profiles obtained from the MCS.

MCS is a radiometer onboard the Mars Reconnaissance Orbiter (McCleese et al., 2007) operating since 2006. It routinely records the thermal infrared emission of the Martian atmosphere in limb and on-planet viewing geometry. Combining the thermal emission recorded at nadir, at different tangent altitudes in limb geometry, and in several channels covering the CO_2 band, allows the retrieval of temperature vertical profiles from 5 to 80 km with a 5 km vertical resolution (Kleinböhl et al., 2009). Due to the Sun-synchronous orbit of MRO, in-track MCS data, acquired when the instrument views the limb in the direction of spacecraft travel, are available at local times of ∼3 a.m. and ∼3 p.m. Cross-track observations, where the instrument views the limb perpendicular to spacecraft travel, are also regularly done at ±1:30 around these two local times. In case of a too high opacity along the line of sight (especially within the aphelion cloud belt or during dust storms), limb retrievals cannot be done, which reduces the vertical coverage of the retrieved profiles down to typically 10–50 Pa (Guzewich et al., 2012; Kleinböhl et al., 2013). Cross-track observations are more impacted than in-track ones, as the latter further exploit planet-viewing observations (for which the line-of-sight opacity is lower) to get complementary constraints on the retrieved profiles. MCS temperature profiles are available on the atmospheres node of NASA's Planetary Data System. For our study, we extract available MCS temperature profiles from version 5.2 in the intervals Ls = 140–168° and from version 5.3.2 for the GDE period (Ls = 197°–212°). As we are interested in evaluating how seasonal changes can impact TIRVIM nadir observations over 50 sols, we first convolve MCS profiles with a Gaussian profile with a full width at half maximum of one scale height, to emulate TIRVIM coarser vertical resolution. We then bin these profiles in Ls (3°-wide bins), latitude (10°-wide bins) and longitude (30°-wide bins) before computing the zonal average of the temperature for each latitude, Ls bin and pressure level, separately for the nighttime and daytime MCS data.

2.3.1. Seasonal Changes Around Ls = 150°

Considering first the Ls = 140–168° period, we note that MCS temperatures show a warming seasonal trend at low and mid-latitudes, both at 3 a.m. and 3 p.m. (see Figure 3). For instance, at 200 Pa, equatorial temperatures increased by +12 K both at 3 a.m. and 3 p.m. over this 45-sol period. This trend is even greater at high southern latitudes, as spring was nearing. On the other hand, high northern latitudes cooled down by ∼8–12 K as autumn was approaching. The seasonal trends estimated separately at 3 a.m. and 3 p.m. differ slightly. This difference is in general smaller than the trend itself (compare for instance the +10 K nighttime trend and the +8 K daytime trend derived at 30 Pa at the equator), so that using an average of the afternoon and nighttime trends, while imperfect in nature, should nonetheless reduce the seasonal bias of TIRVIM data. An exception to this rule is found at high southern latitudes, south of 50°S where for pressures lower than 100 Pa, the 3 a.m. and 3 p.m. seasonal trends differ significantly (compare the rather constant 3 a.m. temperature at 30 Pa, 50°–60°S, with the seasonal increase of +5 K at 3 p.m. at this latitude). This hints to a subtle interplay between seasonal and local time variations at this time of year, likely due to seasonal changes in the tide response as the southern hemisphere eastward jet evolves with season. This will have to be kept in mind when interpreting the results. We also notice that beyond Ls = 160°, seasonal warming occurs faster than in the range 140–160°, especially for pressures lower than 100 Pa. Hence, we choose to fit the MCS temperature anomalies with two linear trends (one for Ls = 140°–158°, the other for Ls = 158°–170°), and use them to de-trend TIRVIM temperature profiles. Equation 1 is then applied to these de-trended temperatures to derive tide characteristics.

2.3.2. MCS Observations During the Global Dust Event of MY34

During the global dust event period covered by TIRVIM (Ls = 197–212°), the atmosphere warmed by typically 5–10 K at 30 Pa (see Figure 4), except at high southern latitudes where a +30 K temperature increase was recorded at 70°S in the afternoon MCS data (+20 K at night). The bulk of the atmospheric warming would be due to absorption of solar radiation by dust; while the significant warming at high southern latitudes is probably

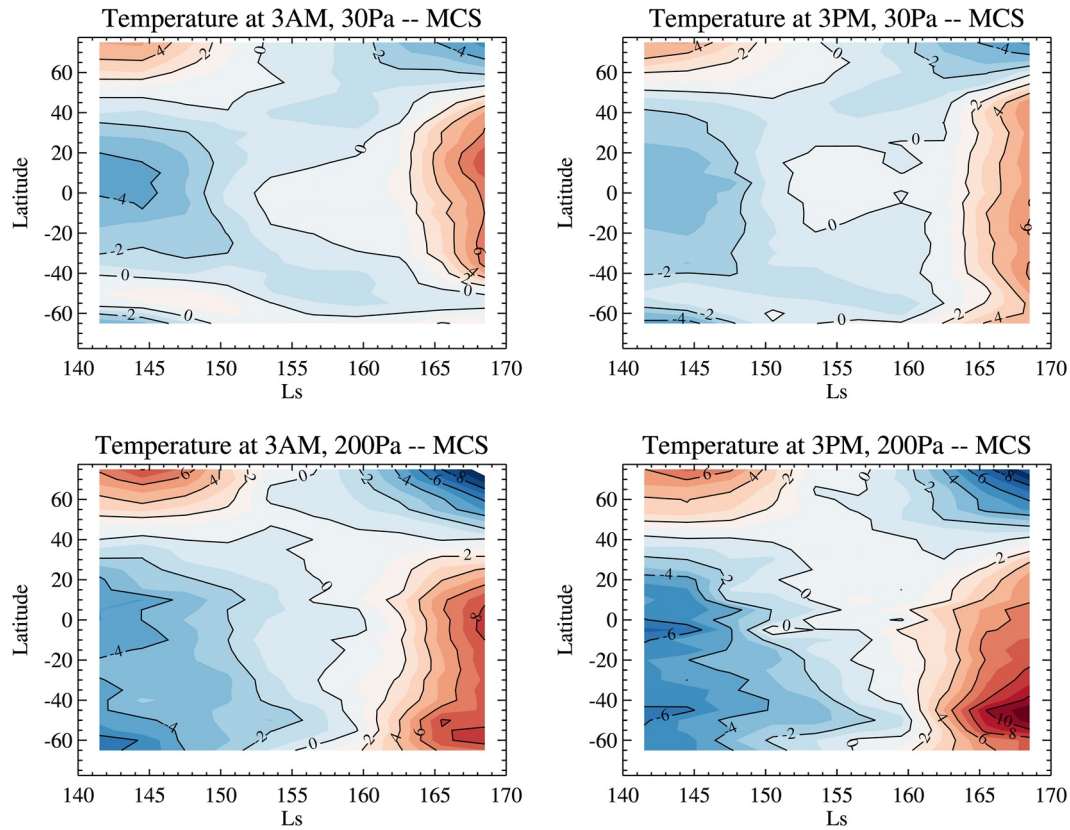

Figure 3. Anomaly (temporal average removed for each latitude bin) of the zonally averaged temperature as recorded by Mars Climate Sounder between Ls = 140° and 168°, binned by 3° in Ls. The temperature anomalies are shown separately at 3 a.m. (left) and 3 p.m. (right) at two pressure levels (30 Pa, upper row and 200 Pa, lower row), with a contour interval of 2 K.

caused by the intensification of the meridional circulation at that time, in response to strong radiative forcing of dust and large amplitude diurnal tides at high southern latitudes (Kleinböhl et al., 2020).

Similar to the pre-dust storm period, we fit the MCS trends with linear functions for each latitude bin and pressure level, de-trend TIRVIM data accordingly and apply Equation 1. We note that the rate of temperature increase differs between day and night at high southern latitudes: at 70°S, afternoon temperatures warmed quickly from Ls = 197°–206° and then only moderately increased, while it was the opposite for nighttime temperatures. We will thus treat with caution the results obtained south of 60°S, due to the complexity of these mingled diurnal and seasonal variations.

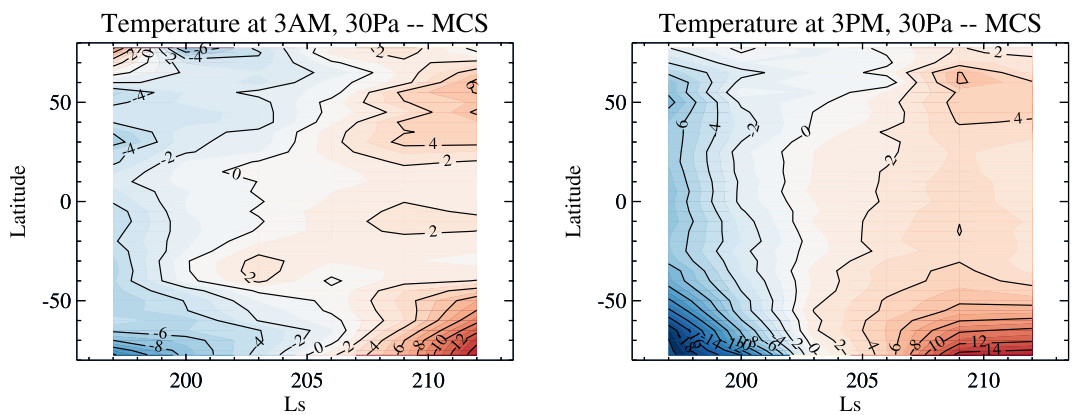

Figure 4. Anomaly (temporal average removed for each latitude bin) of the zonally averaged temperature as recorded by Mars Climate Sounder between Ls = 197° and 212°, binned by 3° in Ls. The temperature anomalies are shown separately at 3 a.m. (left) and 3 p.m. (right) at 30 Pa, with contours drawn every 2 K.

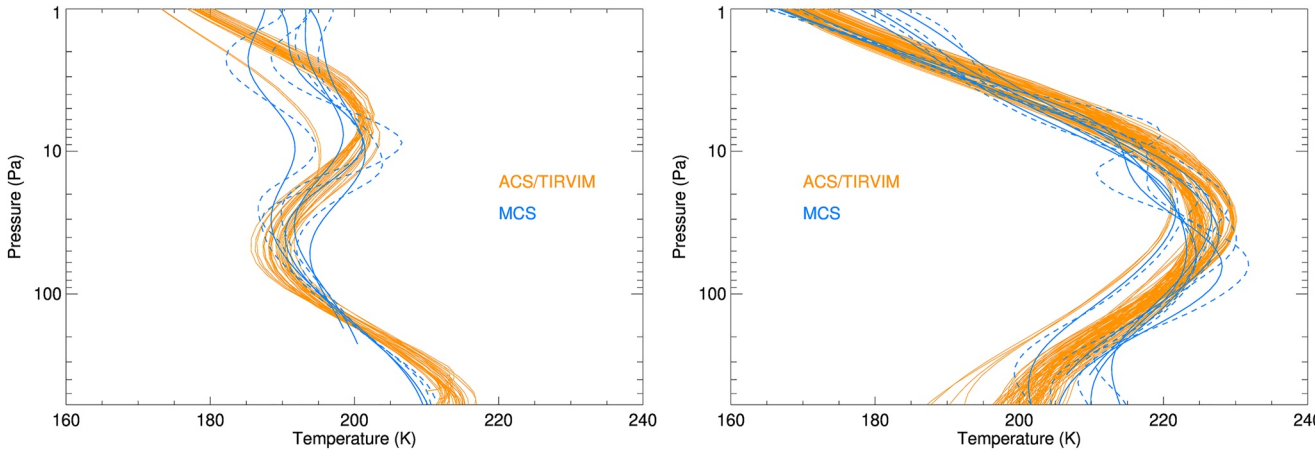

Figure 5. Examples of the good agreement between co-located Mars Climate Sounder (MCS) (in blue) and TIRVIM (in orange) temperature profiles near 45°S, 3 a.m. (left) and 42°N, 3 p.m. (right). Observations are defined co-located when they were acquired less than 30 min apart, 2° in latitude and 6° in longitude apart. Dashed blue lines show the MCS profiles on their native pressure grid while solid blue lines represent vertically smoothed MCS profiles (see text).

2.4. Difference in the Methodology During the GDE

The local time coverage during the MY34 GDE (Ls = 197°–212°) is not as complete as in the previous case study at Ls = 150°. Only half a Martian day, or more precisely, two times 6 hr of local time, are covered over the 25 sols duration of this data set (see Figure 1). In order to slightly improve this point, we added MCS temperature profiles to our data set, providing additional information mostly near 3 a.m. in the southern hemisphere and 3 p.m. in the northern hemisphere. We selected MCS data only within Ls = 210–212°, in line with the Ls—local time coverage of TIRVIM data (see Figure 1). A prerequisite of combining TIRVIM and MCS temperature profiles is to check that there is no bias between the two datasets. A thorough TIRVIM-MCS cross-validation exercise was done for the pre-storm period (Guerlet et al., 2022), showing excellent agreement between the two datasets. To illustrate that this is also the case during the GDE, we present in Figure 5 examples of co-located TIRVIM and MCS temperature profiles near 45°S, 3 a.m. and 42°N, 3 p.m. The vertical atmospheric thermal structure retrieved from MCS shows several cases of temperature inversion that are well captured by TIRVIM, although with a coarser vertical resolution inherent to nadir sounding. Most of the difference between the two datasets fall within error bars (typically 2 K) when TIRVIM coarser vertical resolution is taken into account. Hence in the following, MCS profiles are first vertically smoothed (convolved with a one scale height FWHM Gaussian function, see Figure 5) before the binning procedure.

2.5. Mars Global Climate Simulations

In following sections, we will also compare our results to simulations done with the Mars Planetary Climate Model (PCM, previously known as the Laboratoire de Météorologie Dynamique Global Climate Model or LMD GCM), run with the MY34 dust scenario. We use the standard configuration of version 5 of the PCM, with a resolution of 64 × 48 in latitude × longitude and run with 32 vertical layers, up to 122 km. Among improvements implemented since the work of Forget et al. (1999), the radiative impact of clouds are included (Madeleine et al., 2012) and the water cycle follows that described in Navarro et al. (2014). The model injects dust continuously in the first layer (regardless of time of day) and computes the vertical distribution of dust, while the total column of dust is forced (rescaled) to follow a daily climatology scenario based on MCS dust retrievals for MY34 (Montabone et al., 2020). Temperature profiles are output 24 times per simulated sol. We interpolate and extract model temperature profiles at the same latitudes, longitudes, local times and Ls as all individual TIRVIM soundings. We then emulate the effect of TIRVIM coarse vertical resolution and the influence of the *a priori* temperature profile $\mathbf{T_a}$ used in the retrieval algorithm (which mostly influences the retrieved temperature profiles near the surface and at altitudes above the 5 Pa level) on the GCM profiles by applying the following equation:

$$\hat{\mathbf{T}}_{\mathrm{GCM}} = \mathbf{T_a} + \mathbf{A_k}(\mathbf{T}_{\mathrm{GCM}} - \mathbf{T_a}) \quad (3)$$

with $\mathbf{A_k}$ the averaging kernel matrix, representing the relative weight between the a priori and the observations, and accounting for the vertical resolution of the nadir observations (see details in Guerlet et al., 2022). The $\hat{\mathbf{T}}_{\mathrm{GCM}}$

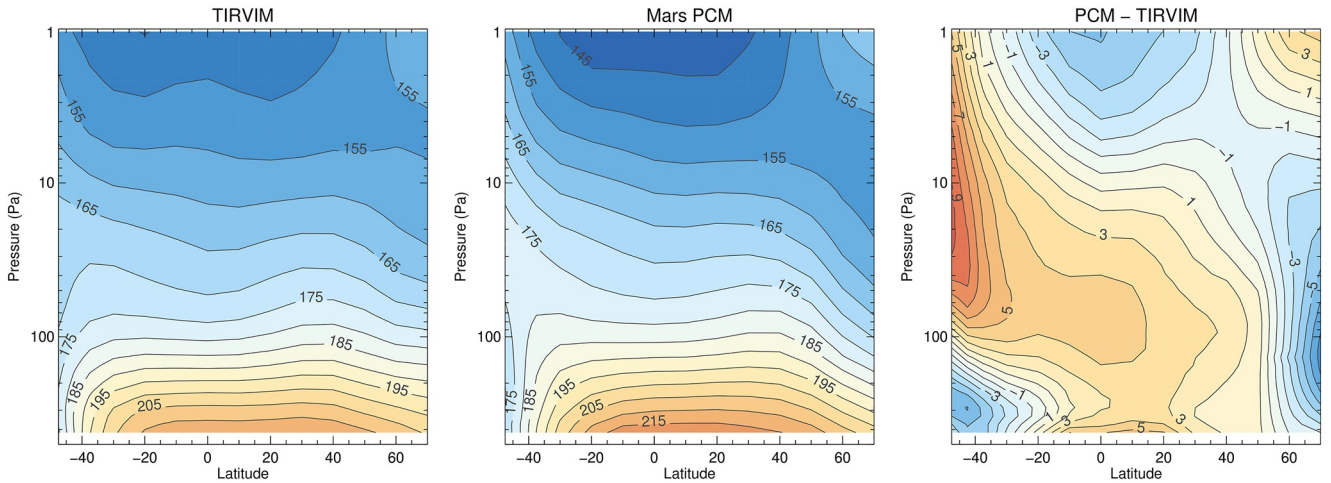

Figure 6. Latitude-pressure cross section of the diurnal mean temperature (T_{avg} in Equation 1) from Atmospheric Chemistry Suite/TIRVIM (left), from the Planetary Climate Model (middle), and the difference between model and observations (right). These figures correspond to Ls ~ 150° and were computed after a seasonal de-trending (see text for details).

profiles are binned in latitude, longitude and local time similarly as TIRVIM data, are zonally averaged, and we perform a seasonal de-trending based on the GCM temperature fields themselves at 3 a.m. and 3 p.m., to mimic the de-trending procedure done on TIRVIM data. We then apply Equation 1 to this binned data set to extract the thermal tides amplitudes and phases.

3. Thermal Structure and Tides for Ls = 150°

3.1. Overview of the Thermal Structure

We first present an overview of the thermal structure obtained at Ls = 150°. The latitude-pressure cross section of the fitted diurnal mean temperature (T_{avg} in Equation 1) is shown in Figure 6. At this season, temperatures in the lower atmosphere ($p > 100$ Pa) are maximal between 20°S and 40°N and decrease sharply toward high southern latitudes (end of winter conditions) and smoothly toward high northern latitudes (end of spring). For instance, at 200 Pa, the daily averaged temperature derived from TIRVIM decreases from a maximum of 197 K at the equator to 174 K at 50°S, 193 K at 50°N and 189 K at 70°N. Overall, temperatures from the model are in good agreement with the observations: differences between the two lie within ±4 K for most of the latitude-pressure domain. We note that the Mars PCM predicts steeper equator-to-pole gradients in the lower troposphere, with for instance a minimum temperature of 170 K at 50°S for a maximum temperature of 200 K near the equator at 200 Pa.

At higher altitudes, the daily averaged temperatures are characterized by a tongue of warmer air at mid- and high southern latitudes, as adiabatic warming from the descending branch of the Hadley circulation cells takes place. Between ~5 and 100 Pa, near 40–50°S, the PCM predicts a significantly stronger warming than that observed. This observation-model mismatch might reflect inadequacies in the model, such as an erroneous dust vertical distribution and/or a too strong meridional circulation in the Mars PCM at this season. However, we recall that at 40–50°S, the seasonal de-trending based on MCS data applied to TIRVIM retrievals is quite uncertain, due to different daytime and nighttime seasonal trends seen in MCS temperatures. Part (3 K out of 4 K) of the PCM-TIRVIM mismatch could thus be attributed to uncertainties (of the order of 3 K) in de-trending the observations.

3.2. Overview of Local Time Variations

The zonally averaged temperature variations with local time and latitude are shown at three pressure levels in Figure 7. At low altitudes/high pressure levels (200 Pa), the temperature is found maximum near 10°S and 3 p.m. (205 K). Peak-to-peak local time variations reach an amplitude of ~12 K. Apart from the difference in equator-to-pole gradients mentioned above, the Mars PCM temperatures are in good agreement with TIRVIM and also exhibit a local maximum near 3 p.m. at low latitudes.

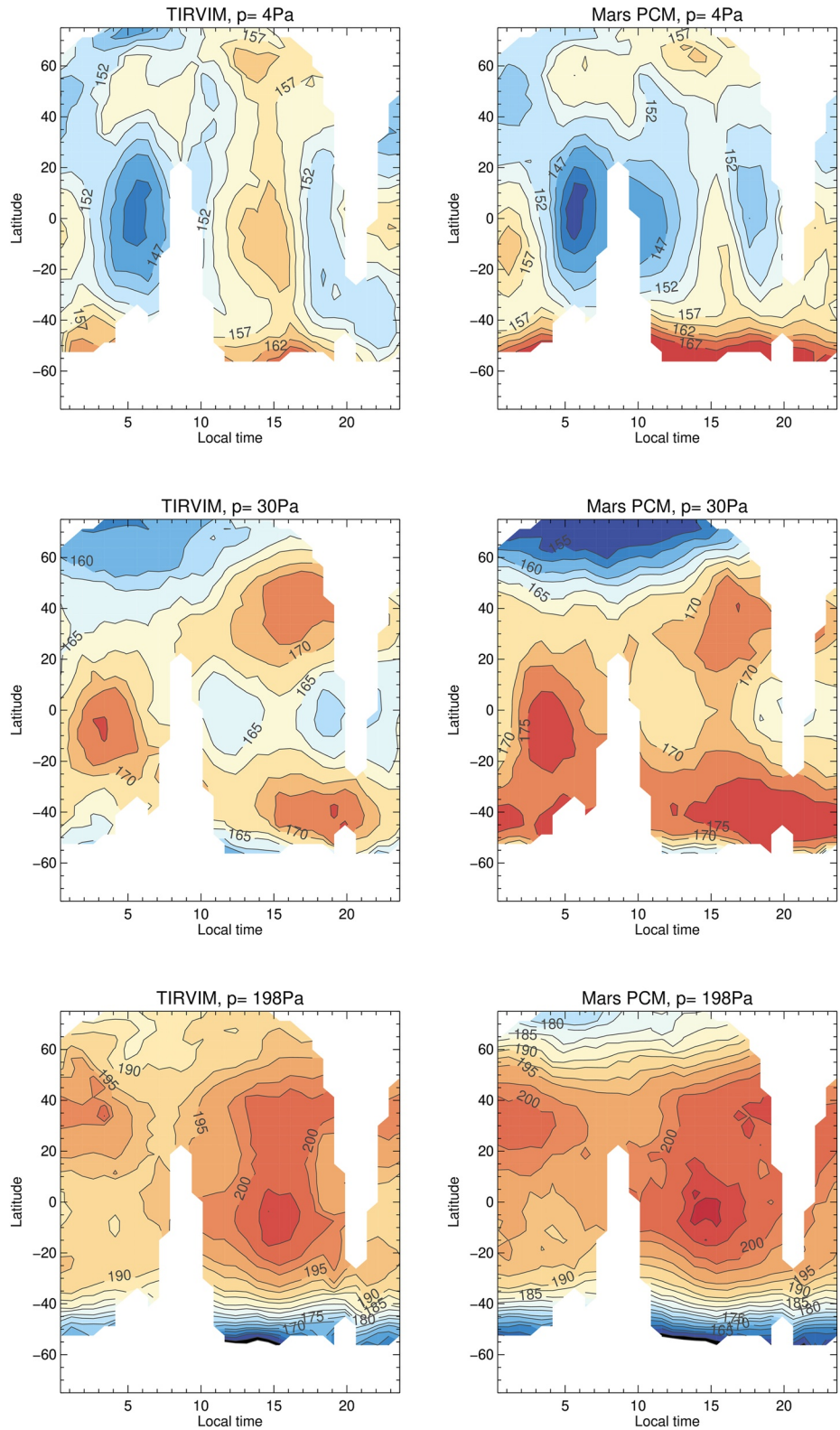

Figure 7. Zonal mean temperature with latitude and local time at 4 Pa (top), 30 Pa (middle) and 200 Pa (bottom), at Ls ~ 150°. The left column corresponds to Atmospheric Chemistry Suite (ACS)/TIRVIM observations, the right column to the Mars Planetary Climate Model simulations, sampled at ACS/TIRVIM latitudes, longitudes, times and convolved to ACS/TIRVIM vertical resolution ($\hat{\mathbf{T}}_{PCM}$ in Equation 3). To generate this figure, the data was binned by 5° in latitude and 30 min in local time. Contours are drawn every 2.5 K (labeled every 5 K).

At middle altitudes (30 Pa, approximately 30 km above the areoid), the diurnal variations in temperature reveal a different pattern. Near the equator, the temperature is found to be maximum near 3 a.m. and minimum near 7 p.m. This feature of warm nighttime temperatures at this altitude is well known and is a manifestation of the vertically propagating nature of the diurnal thermal tide in the tropics (Lee et al., 2009). The fact that these two temperature extrema are not separated by 12 hr is a first hint that the thermal field is also influenced by a semidiurnal tide (note that a second local temperature minimum is located near noon), as we will see in the next section. The modeled temperature field exhibits a similar diurnal trend at low latitudes, although with systematically warmer temperatures. At higher latitudes, the temperature is found to be maximum near 3–8 p.m. at both 40°N and 40°S, with a rather symmetric structure about the equator. In the Mars PCM, the local maximum near 45°S at 6 p.m. is significantly warmer than its northern counterpart, and the high northern latitudes are also much colder than that observed by TIRVIM: this reflects the overall PCM-TIRVIM discrepancy in meridional trends seen in the diurnal average of the temperature discussed earlier (see Figure 6).

At low pressures (4 Pa, nearly 50 km altitude), the thermal structure is more complex. The general trend of decreasing temperature from equator-to-pole is absent at this pressure level, and is replaced by a family of local temperature extrema. Indeed, the coldest temperatures are not found at high latitudes (contrary to lower altitudes) but at the equator, at 6 a.m. (both in the observations and the Mars PCM). A semidiurnal pattern is also clearly seen near the equator. To go beyond this qualitative analysis, we discuss below the amplitudes and phases of the migrating thermal tides and how well they are reproduced in the model.

3.3. Thermal Tides at the Equator

Both the diurnal and semidiurnal tides are expected to have significant amplitudes near the equator. As a case study, we detail below the results regarding the equatorial bin (−5°; +5°). The observed temperature diurnal anomalies and the fitted diurnal and semidiurnal components of the migrating tides at all pressure levels are presented in Figure 8. At the equator, the amplitude of the diurnal tide is found to be locally maximum near 50 and 3 Pa with values of 4.9 and 5.2 K, respectively. The semidiurnal tide is maximum over the range 2–10 Pa, where its amplitude is in the range 4–5.5 K. Examples of best fits to TIRVIM temperatures, along with the different contributions of the diurnal and semidiurnal modes, are shown in Figure 10 at 50 and 10 Pa. Our results clearly assess the downward phase propagation of both the diurnal and semidiurnal tides, which is consistent with upward group velocity for inertia-gravity waves and complies with tidal theory (Forbes, 1995; Lindzen & Chapman, 1969). We also derive a much longer vertical wavelength for the semidiurnal tide compared to the diurnal tide, which is also expected. Corresponding vertical wavelengths amount to 4.5 scale heights (H) for the diurnal tide and 7.8 H for the semidiurnal tide (see Figure 9). These values are very close to that predicted by the Mars PCM: 4.8 H for the diurnal mode, 7.8 H for the semidiurnal mode, increasing to 9.6 H if we consider the model results on their own latitude, longitude, local time and pressure grid instead of the co-located and vertically convolved model outputs.

A characteristic feature of the diurnal tide not well captured by TIRVIM is the expected large amplification of the vertically propagating component of tide with altitude, as atmospheric density exponentially decreases. This is well visible in the amplitudes derived from the modeled temperature field at the native vertical resolution of the Mars PCM (see the central row of Figure 8), where the amplitude of the diurnal tide reaches 10–12 K at 1–2 Pa. Amplitudes of 6–12 K have previously been reported at this pressure level from MCS data analysis (Kleinböhl et al., 2013; Lee et al., 2009; Steele et al., 2021), however, in TIRVIM retrievals, the amplitude of the diurnal tide seems to decrease above the 3 Pa level. This apparent disagreement is an example of a shortcoming in TIRVIM nadir observations: above the ∼5 Pa pressure level, the information content decreases and the retrieved temperature profile smoothly goes back to the a priori profile. TIRVIM vertical resolution is also coarser at this pressure range (1.5–2 scale height), which leads to an underestimation of the vertical oscillations that characterize the tides.

When TIRVIM information content is taken into account, the amplitudes of the diurnal and semidiurnal tides derived from $\hat{\mathbf{T}}_{\mathrm{PCM}}$ are in fair agreement with TIRVIM ones (see the bottom row of Figure 8), although we find a slightly stronger diurnal tide at 50 Pa in TIRVIM data compared to $\hat{\mathbf{T}}_{\mathrm{PCM}}$. This result is considered robust, as the amplitude of the tide at 50 Pa in the Mars PCM is the same whether we consider $\mathbf{T}_{\mathrm{PCM}}$, $\hat{\mathbf{T}}_{\mathrm{PCM}}$ or even the "raw" model outputs at Ls = 150° on their native latitude, longitude, pressure and local time grid (i.e., without selecting profiles co-located with TIRVIM observations nor any vertical smoothing). The amplitude of the semidiurnal tide

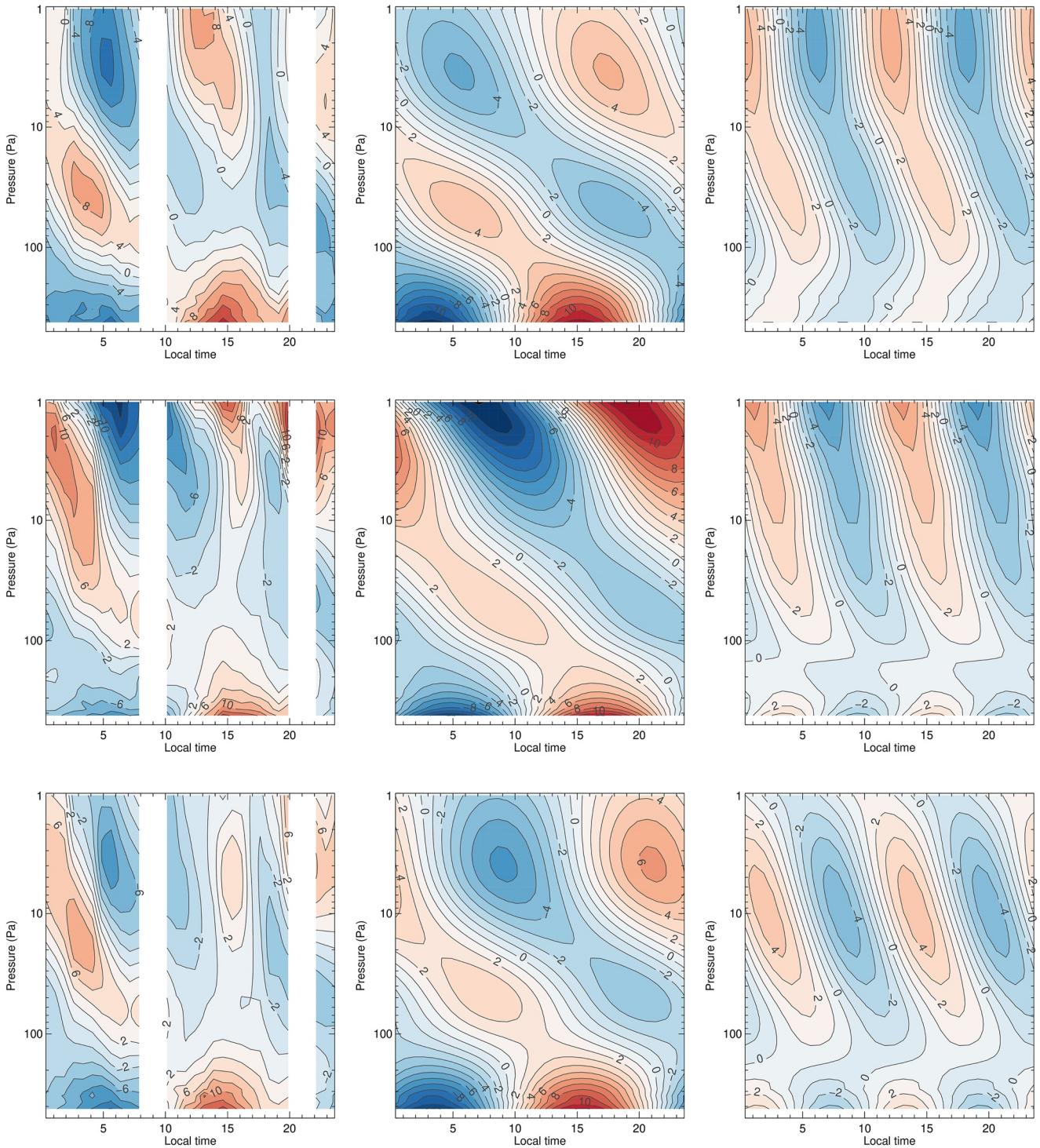

Figure 8. Left: Diurnal anomaly of the zonally averaged temperature in the bin (−5°,5°) at Ls ∼ 150°; middle: reconstructed diurnal mode of the migrating thermal tides from the fitted parameters in Equation 1; right: reconstructed semidiurnal mode. The top row corresponds to Atmospheric Chemistry Suite/TIRVIM retrieved temperatures, the middle row to predictions by the Mars Planetary Climate Model sampled at TIRVIM latitudes, longitudes and times on its native vertical grid, and the bottom row shows the same model results convolved to TIRVIM vertical resolution ($\hat{\mathbf{T}}_{\mathrm{PCM}}$ in Equation 3).

is found to be similar between TIRVIM and the Mars PCM, except that our derived amplitude is stronger than the modeled one for $p < 10$ Pa. Actually, the semidiurnal tide amplitude derived from TIRVIM is similar to the one in the Mars PCM obtained without vertical smoothing. We note however that the difference between the

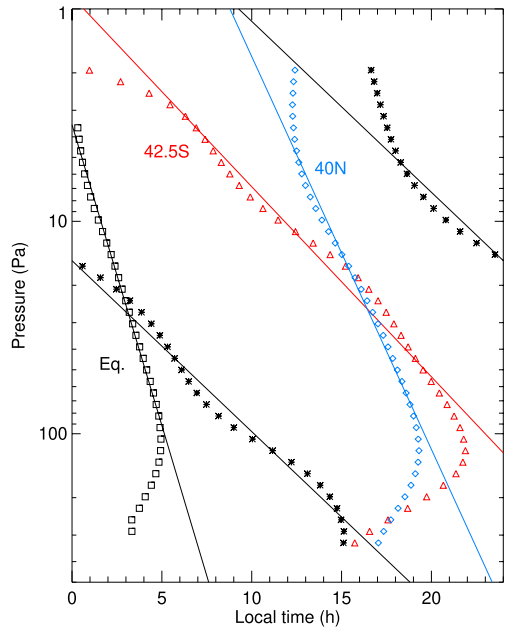

Figure 9. Phase of the diurnal (black stars) and semidiurnal mode (black squares) at the equator, with pressure, at Ls = 150°. The vertical wavelength is estimated from linear fits excluding the lowest and highest levels, shown as solid lines. Phases of the diurnal mode for the bin 40N (blue diamonds) and 42.5S (red triangles) are also shown for comparison.

two modeled fields (vertically smoothed or not) is small in the case of the SW2 amplitude, owing to its larger vertical wavelength. Finally, note that near 1–5 Pa, the semidiurnal tide amplitude derived from TIRVIM at the equator is commensurate, or even greater, than the diurnal mode. This is not the case in the PCM results, where the DW1 tide amplitude is greater than that of SW2.

The seasonal de-trending has an important effect: without it, the amplitude of the semidiurnal tide derived from TIRVIM would amount to 6.4 K at 10 Pa (instead of 3.8 K). That is easily explained: as the background seasonal temperature increases over the course of the 45 sols considered here (see Figure 3), and as TIRVIM acquired data at two local times 12 hr apart per TGO orbit (drifting in local time with Ls), this seasonal increase can be wrongly interpreted as a warming occurring with local time, with two extrema per day: in other words, seasonal warming is aliased with the semidiurnal tide mode. This aliasing effect was already suspected by Fan, Guerlet, et al. (2022), who analyzed TIRVIM observations near Ls = 90° of MY35 without seasonal de-trending. Removing seasonal trends before decomposing the tide harmonics yields a more realistic amplitude of the semidiurnal tide.

Regarding the phases of the tides, and taking 30 Pa as an ad hoc reference pressure level, the temperature maximum associated with the diurnal tide is found to occur at 4:30 a.m. in the observations and to occur slightly later, near 6:00 a.m., in the modeled field $\hat{\mathbf{T}}_{\mathrm{PCM}}$ (or 5:40 a.m. in the raw model outputs). Such a ∼1 hr 30 min phase shift between model and observations was also reported by Fan, Guerlet, et al. (2022) near Ls = 90° of MY35 and is currently under investigation. It could be related to unrealistic aerosol vertical distribution (hence radiative forcing), both for dust and water ice clouds. Indeed, at Ls = 150°, water ice clouds likely account for a significant part of the thermal forcing (Haberle et al., 2019; Wilson et al., 2014). Another possible shortcoming is related to regional circulations, or topography-related circulations, not fully resolved by the PCM. We also note that at this season, topographically generated Kelvin waves are known to interfere (destructive or constructive interferences) with the Sun-synchronous tides (Wilson & Hamilton, 1996); studying these tides, their interactions, and how well they are represented in the Mars PCM is deferred to future studies. Regarding the phase of the semidiurnal tide, we find an excellent agreement between model and observations (less than half an hour difference, which is of the order of our bin size, hence not significant). Should we not seasonally de-trend the TIRVIM temperatures, we would find a 2 hr 40 min phase difference between model and observations, similar to the 3-hr phase shift reported by Fan, Guerlet, et al. (2022) for the semidiurnal tide at Ls = 90° that these authors derived from their TIRVIM analysis with no seasonal de-trending.

3.4. Comments on Uncertainty Estimates

Uncertainties on the derived tide amplitudes result from a combination of several factors: from measurement errors on the retrieved temperatures; from the incomplete local time coverage; from errors on computing the zonal averages (due to uneven sampling in latitude within a bin, or in longitude among the bins); and from seasonal trends mingled with local time variations that are not perfectly accounted for. The observational precision (not accuracy) is estimated to 0.5–1 K and that on the seasonal de-trending is estimated to 1–2 K depending on latitude, by looking at the differences between the 3 a.m. and 3 p.m. trends derived from MCS. Setting a nominal 1-σ uncertainty of 1.5 K for the zonally averaged temperature thus seems reasonable. If the zonal coverage is incomplete (we allow for one to three bins out of 18 to be missing), we artificially increase this value by quadratically adding a fraction of the variance among the longitude bins at a given latitude, as there is a risk that strong waves (non-migrating tides) are not fully canceled and contribute to the averaged temperature.

The resulting reduced χ^2 values are close to unity (ranging between 0.5 and 1.5) for all latitude bins for $p > 10$ Pa, and residuals are also smaller than 1.5 K, which suggests that these measurement uncertainty values are of the right order of magnitude. Note that before seasonal de-trending, the χ^2 values were up to four times larger at low latitudes and near 50°S, which re-enforces the necessity of this approach. The quality of the fit nonetheless decreases toward lower pressure levels, reaching on average a χ^2 of 2.5 at 2 Pa. Indeed, residuals of typically 2 K

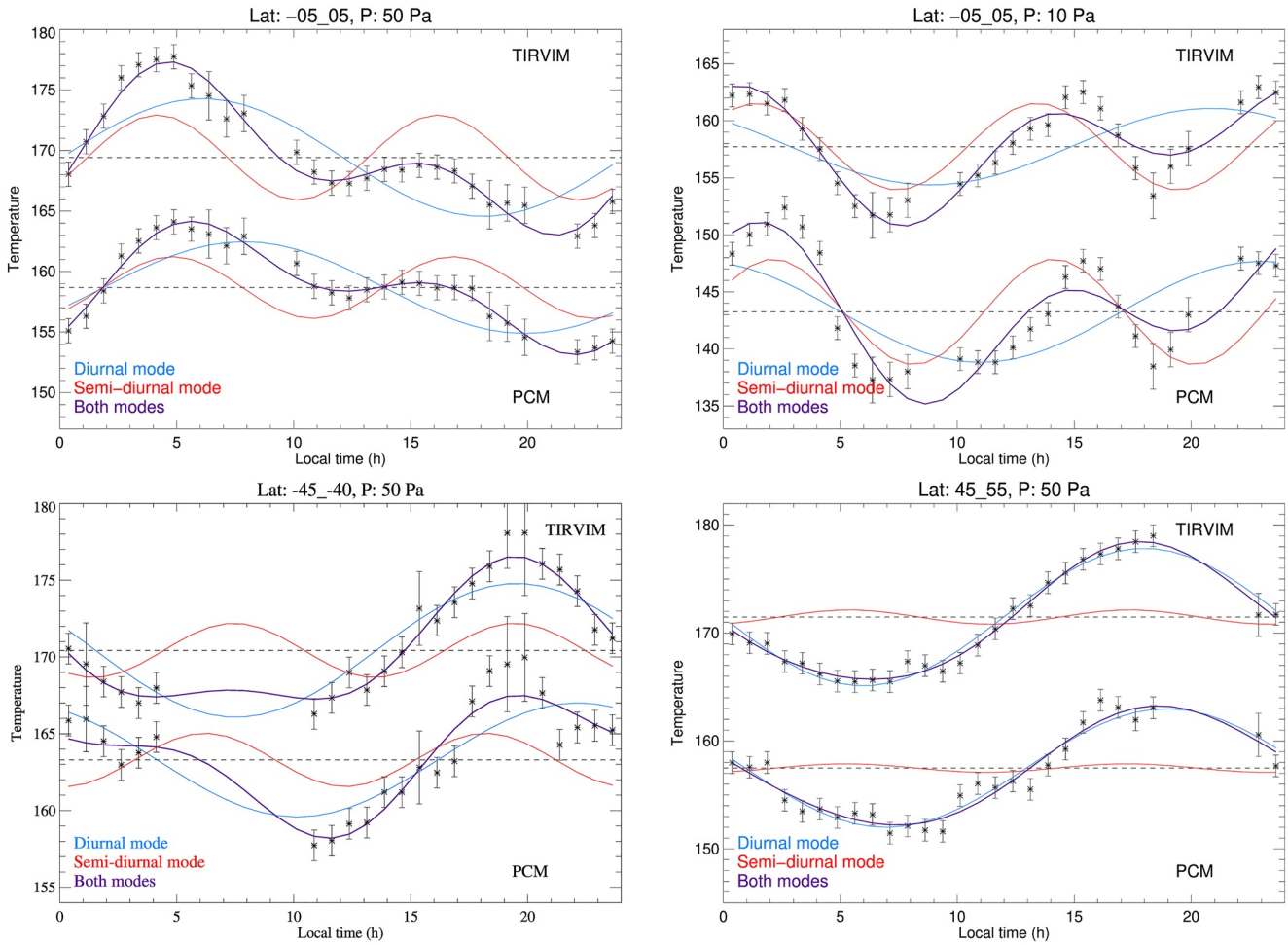

Figure 10. Zonally averaged temperature as a function of local time as measured by TIRVIM (or computed from $\hat{\mathbf{T}}_{\mathrm{PCM}}$, shifted by −15 K in each panel) at Ls ∼ 150°, shown as black stars at different latitude bins and pressure levels, as labeled. The fitted diurnal mean temperature is shown as a horizontal dashed line while the colored lines represent the fitted contributions from the diurnal (in blue) and semidiurnal (in red) modes. Best fits to the data are shown in purple.

are present at low pressure levels, which origin is not clearly established but is likely due to imperfect seasonal de-trending.

Given these observational uncertainties, the formal error on the fitted tide amplitudes are of the order of 0.3–0.4 K. However, this error is underestimated for several reasons. First, it is important to note that the tide amplitude themselves are expected to vary over the course of the 45-sol period considered here (between sol 304 and 349). For instance, considering the "raw" PCM outputs at sols 304, 319, 334, and 349, we find that the diurnal tide amplitude at the equator changes by typically 1 K (up to 2 K for $p < 10$ Pa), and that of the semidiurnal tide by 0.5 K (1 K for $p < 20$ Pa), among these 4 selected sols. Second, we note that a terdiurnal thermal tide exists in the "raw" PCM outputs, with amplitudes in the range 0.2–0.6 K for pressures lower than 30 Pa. However, this mode is not detected neither in TIRVIM nor in the $\hat{\mathbf{T}}_{\mathrm{PCM}}$ fields when we add it in Equation 1, confirming that even without any measurement error, the uncertainty on tide amplitudes due to uneven spatio-temporal sampling is at least 0.6 K. Fan, Forget, et al. (2022) did detect the terdiurnal mode using temperature profiles derived from another nadir-viewing spectrometer, EMIRS, onboard the Emirates Mars Mission. The authors could reach a higher precision thanks to the observing scheme that acquires observations at all local times within a few sols only. Finally, we can also estimate the precision on tide amplitudes by comparing that derived from the Mars PCM temperature field but sampled on TIRVIM observational grid versus the temperature on the regular model grid on a given sol, to evaluate the impact of incomplete spatio-temporal coverage as well as imperfect seasonal de-trending. This difference is of the order of 1 K for $p > 20$ Pa and increases to 2 K at 1–3 Pa. The latter values are thus taken as our precision estimates for tide amplitudes derived from TIRVIM.

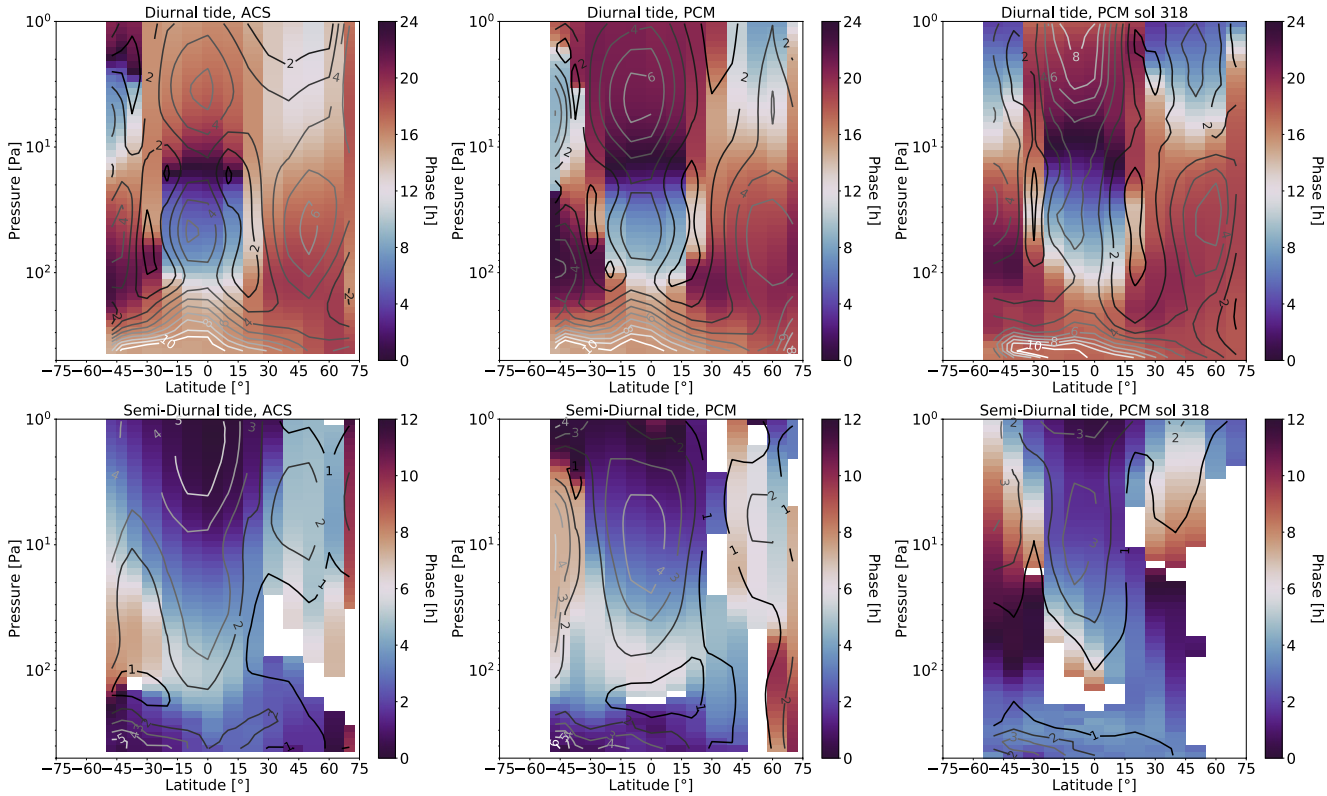

Figure 11. Phase (color, in hours) and amplitude (contour, in Kelvin) of the two main migrating tide harmonics at Ls ∼ 150° (top row: diurnal, bottom row: semidiurnal harmonic). The left column corresponds to Atmospheric Chemistry Suite/TIRVIM temperatures, the middle one to $\hat{\mathbf{T}}_{\mathrm{PCM}}$ and the right one to the Mars Planetary Climate Model on its native latitude, longitude and pressure grid at sol 318. Blank areas indicate regions where the derived SW2 tide amplitude was less than 0.5 K, making phase determination unreliable.

In addition to these precision values, one has to keep in mind the poorer accuracy of the observations at low pressure levels, due to the limited information content and coarse vertical resolution. Absolute tide amplitudes derived from nadir observations can be underestimated by a factor of 2 for $P < 10$ Pa as discussed in the previous section. However, when comparing similar quantities (e.g., $\hat{\mathbf{T}}_{\mathrm{PCM}}$), a precision of ∼1–2 K on tide amplitudes should nonetheless be reached.

3.5. Tide Amplitudes and Phases at All Latitudes

Amplitudes and phases of both harmonics of the migrating tides are reported in Figure 11 as a function of latitude and pressure. We focus here on the meridional and vertical structure of the tide harmonics, which can be represented by a combination of Hough functions, according to classical tidal theory. In the tropics (15S–20N), the DW1 signature is characterized by a vertically propagating component with downward phase propagation and amplitudes of typically 3–4 K. This meridional structure is a characteristic feature of the (1,1) Hough function that corresponds to the main vertically propagating component of DW1, peaking at the equator and dominating at latitudes <30°. At high latitudes (>60°), classical theory predicts a domination of vertically trapped Hough modes that are typically amplified within the westerly jets, and for which the temperature response is effectively confined to the height range of dominant (aerosol) thermal forcing. At mid-latitudes (40–50°), the diurnal tide would be both influenced by these high latitude vertically trapped Hough modes, and by the extra-tropical part of the (1,1) vertically propagating mode. The (1,1) mode indeed has significant negative nodes peaking at 30° latitude (see for instance Figure 2 in Wu et al., 2021). Here we report two distinct signatures at mid-latitudes depending on the considered hemisphere. On the one hand, at latitudes 30–50°S, the DW1 signature exhibits downward phase propagation, shifted by about 14 hr compared to the equator, with amplitudes of 2–3 K. The vertical wavelength derived near 40°S and at the equator is similar and amounts to 4.8 H (see also Figure 9). This implies that the leakage of the tropical (1,1) Hough mode is clearly dominant in the winter hemisphere, and that

the vertically trapped modes do not influence significantly the mid-latitudes at this season. On the other hand, near 30–60°N, although we do report a downward phase propagation behavior as well, the vertical wavelength is found to be larger: it ranges from 10 H (at 40°N) to 14 H (at 60°N). The tide amplitude is also larger (4–6 K) and peaks near 45–50° latitude. This suggests a competition between several Hough modes at summer mid-latitudes. Such a north-south asymmetry in the vertical wavelength of DW1 in TIRVIM observations indicate differences in tidal forcing (radiative forcing by aerosols for instance) and/or point to an alteration of the meridional structure of the Hough functions by the background zonal mean wind (classical tide formalism assumes no background zonal wind). These hypotheses remain to be explored quantitatively. On the other hand, the DW1 phase structure in the Mars PCM (on its native grid or considering $\hat{\mathbf{T}}_{\mathrm{PCM}}$) appears (a) more symmetric about the equator and (b) dominated by the (1,-2) vertically-trapped Hough mode in particular in the northern hemisphere, with a maximum amplitude at 60°N and an almost constant phase from the surface to $p = 10$ Pa at this latitude.

Regarding the semidiurnal harmonic, we first caution that the tide amplitudes derived from ACS/TIRVIM poleward of 40°N are small (less than 1 K in general), which results in poor confidence in the determination of its phase. Furthermore, we note strong differences in the tide phases derived at high latitudes between the Mars PCM on its native pressure grid at one sol (318) and the ones estimated from $\hat{\mathbf{T}}_{\mathrm{PCM}}$ sampled at TIRVIM locations, local time and Ls. This implies that estimating the phase of SW2 is very sensitive to the observation scheme at latitudes poleward of 40°, and we cannot interpret these results. On the other hand, the broad equatorial maximum (in amplitude) of SW2 between 30°N and 30°S seems a robust feature and is similar in TIRVIM and the Mars PCM. It shows slow downward propagation, corresponding to the (2,2) Hough mode that is expected to dominate the SW2 tide structure.

Finally, we note that the overall latitudinal pattern of the thermal tide is not strictly symmetric about 0° but is slightly shifted toward the southern hemisphere, with local maximum amplitudes of both the diurnal and semidiurnal tides centered at 5–10°S. This feature is also present in the Mars PCM simulations and is also predicted by other climate models. Indeed, using MarsWRF, Lee et al. (2009) reported a seasonal dependence of both the amplitude and the location (in latitude) of the peak of the 3 p.m.–3 a.m. temperature difference, being maximum and centered near 15°S at Ls = 90°, minimum and centered near 15°N at Ls = 270°, and centered at 0° latitude at Ls = 0° and 180°. Our analysis at Ls = 150° matches well this prediction. Another GCM study (Wilson & Hamilton, 1996) also noted that the vertically propagating components of the tide harmonics tend to be ducted into the winter hemisphere. Classical tide theory predicts modes (Hough functions) that are centered at the equator, but this framework assumes zero background zonal wind. In the Earth atmosphere, the tide's amplitude and phase have been shown to be very sensitive to the absolute vorticity, that is, the sum of the Coriolis parameter and the relative vorticity, linked to latitudinal wind shears in the mean zonal wind (McLandress, 2002). Although the Coriolis parameter is null at the equator, this is not the case of the absolute vorticity, due to zonal wind shears: as a result, the dynamical equator is not centered at zero latitude throughout the year, but is slightly ducted into the winter hemisphere. This might explain why the maximum tides' amplitudes also follow such a latitudinal trend with seasons.

3.6. Comparisons to Previous Observations and Discussion

Comparison with previous nadir soundings, for this specific season, are limited. From TES aerobraking data, Banfield et al. (2000) estimated the amplitude of the diurnal tide to be of the order of 4 K at an altitude of 3–4 scale height, at 40°S for Ls = 180° during MY23. This is similar to the one derived here by TIRVIM at Ls = 150° and 30 Pa (∼3 scale heights). Unfortunately, TES aerobraking data were too sparse to correctly determine the tides' characteristics at low latitudes (Banfield et al., 2000). Using TES nadir observations from the nominal mission, acquired near 2 a.m. and 2 p.m., Banfield et al. (2003) performed a wave mode decomposition. However, with only two local times, the thermal tides are aliased and the amplitude and phase of the sun-synchronous diurnal tide cannot be derived properly.

Regarding limb measurements, MCS data available at this season and same Martian year (MY34) were almost exclusively acquired near 3 a.m. and 3 p.m. (see Figure 1). In a previous study, a comparison of TIRVIM temperature profiles with a set of co-located data from MCS (acquired at ± one sol, less than 3° away in latitude, 6° away in longitude and 30 min away in local time) has revealed an excellent agreement between the two data sets, shown in Guerlet et al. (2022) as part of a cross-validation exercise. From this study, the 3 p.m.–3 a.m. peak-to-peak temperature difference amounts to ∼8 K in TIRVIM data and to 10 K in MCS data at 40 Pa, corresponding to tide

amplitudes of 4–5 K (assuming that the diurnal tide extrema peaks near 3 a.m. at this pressure level). Previous investigations from MCS at the same season (Ls = 135–165°) in MY28 reported a peak-to-peak 3p.m.–3a.m. temperature difference between 5 and 10 K at the equator and 30 Pa (a T_{diff} value between 2.5 and 5 K, Lee et al., 2009), which is commensurate to our findings. We caution however that the 3 p.m.–3 a.m. temperature difference cannot be completely trusted as an absolute measure of the peak-to-peak amplitude of the diurnal tide, as it is impossible to know the timing of the temperature extrema from these two local times alone. This is particularly true near 50°N at Ls = 150°: here, DW1 is found to have a maximum amplitude near 30 Pa, with temperature extrema occurring near 6 hr (and not 3 hr), so that taking the 3 p.m.–3 a.m. temperature difference would underestimate the diurnal tide amplitude. This represents a relatively small error, but if the phase of the thermal tide is even more shifted or changes with seasons (significant interannual variations of the tide phases have indeed been reported by Steele et al. (2021)), the 3 p.m.–3 a.m. temperature difference then becomes a poor metrics of the tide amplitudes.

Identifying the semidiurnal tide from along-track MCS data alone is not possible, as only two local times are available. More precise estimates of the tide amplitudes and phases (for both the diurnal and semidiurnal tides) can be derived by combining along-track and cross-track MCS data, covering altogether six different local times per day. This strategy has been exploited by Kleinböhl et al. (2013), Wu et al. (2015, 2021), and Steele et al. (2021). However, at low to mid-latitudes, the MCS local time coverage is limited to ±1.5 hr from 3 a.m. or 3 p.m., resulting in a large local time range without coverage over which one has to interpolate. Small errors in the temperature profiles can lead to large uncertainties when decomposing the tides' parameters. For instance, Kleinböhl et al. (2013) estimated the semidiurnal tide amplitude to be 6–8 K in the 1–10 Pa equatorial region at Ls = 100° of MY31, but with a 5 K uncertainty. We also note that the vertical coverage of temperature profiles obtained from MCS observations (along and cross-track) can be severely limited in the lower atmosphere due to aerosols, which is often the case at equatorial latitudes where the semidiurnal tide is expected to peak, limiting the determination of semidiurnal tide parameters to pressures lower than ∼30 Pa. At higher latitudes (beyond 60°), the local time range covered by MCS increases based on the measurement geometry, leading to a more robust determination of tide parameters. The same authors derived a greater amplitude of the semidiurnal tide at winter high latitudes (60°S); unfortunately, our results are limited to mid-latitudes (40°S) and we cannot make such a comparison here. Wu et al. (2015) extended this work to two full Martian years. Their derived tide amplitudes are in good agreement with ours at Ls = 150° (for MY31): they report a 4–5 K amplitude for the diurnal tide near 30 Pa and an increasing amplitude with height of the semidiurnal mode, ranging from 2 ± 2 K to 5 ± 2 K going from 10 to 2 Pa (note that this 2 K uncertainty is likely underestimated due to uneven local time sampling). Regarding the meridional structure of the phase of DW1, our results agree qualitatively with that of Wu et al. (2021), shown at Ls = 90° and 180° for MY33, with mid-latitudes (30–60°) showing downward phase propagation similarly to what is seen in TIRVIM data. However, no strong north/south asymmetry in the vertical wavelength is reported by the authors, which might be a phenomenon specific to the season (Ls = 150°) and/or MY studied here.

These favorable comparisons show that the study of migrating thermal tides, which have long vertical wavelengths, with a nadir-viewing sounder, lead to quantitatively robust results—at pressures greater than ∼5 Pa—despite its rather coarse vertical resolution. This is very complementary to what MCS data analysis can achieve. Our results confirm previous findings that semidiurnal tides are important even in seasons of low to moderate dust amounts (Kleinböhl et al., 2013). The authors had shown that the radiative effect of clouds was an important driver of the semidiurnal mode, resulting in strong amplitudes of SW2 at high altitudes (10–12 K at 1 Pa) and a moderate 4 K amplitude at the equator down to 50 Pa (consistent with our observations). The important role of clouds on forcing SW2 was also highlighted by Wilson et al. (2014) and Haberle et al. (2019) who showed a continuous effect in the aphelion season, even at Ls = 150°. Our results thus seem to confirm this prediction. The height of the cloud deck will be centered at a higher altitude at Ls = 150° due to the warming of the atmosphere relative to Ls = 100°. Interestingly, a re-analysis of the tide amplitudes from TIRVIM at Ls = 90° (first shown in Fan, Guerlet, et al., 2022), with seasonal de-trending applied, reveal a 3 K equatorial semidiurnal tide amplitude for $p < 10$ Pa. The stronger, 4–5 K SW2 amplitude at $p < 10$ Pa at Ls = 150° might align with cloud radiative forcing being shifted to higher altitudes.

We remind that the Mars PCM does include such radiative forcings by clouds. The fact that the PCM reproduces qualitatively the observed semidiurnal tide amplitude and phase (in the range 30°S–30°N where TIRVIM results are the most reliable) indicates that these forcings are well taken into account, at least to first order.

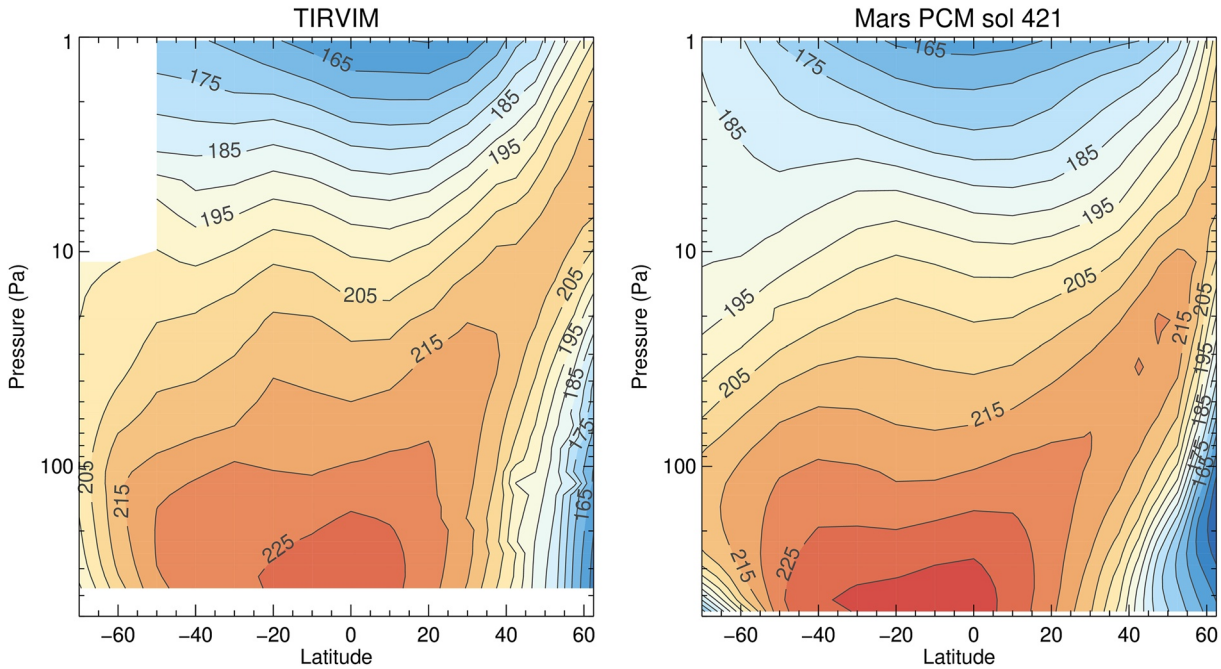

Figure 12. Latitude-pressure cross section of the diurnal mean temperature derived from Atmospheric Chemistry Suite/TIRVIM (left) and as predicted from the Mars Planetary Climate Model (PCM) (right) during the global dust event of MY34. We show here the Mars PCM output corresponding to sol 421 (Ls = 208°), that is, a few days later than the middle of our observation period, as there is a lag of a few sols in the simulated dust distribution compared to Mars Climate Sounder observations (see for instance Figure 12 in Young et al. (2022)). Choosing a slightly earlier or later date does not change our results.

4. Thermal Structure and Tides During the Global Dust Event

With visible dust column optical depth greater than two over most of the Martian globe for more than 60 sols (Kass et al., 2020), the global dust event of MY 34 significantly impacted the dynamics and thermal structure of its atmosphere. Below we report on the diurnal average temperature derived from TIRVIM during the storm as well as the corresponding migrating tide parameters.

4.1. Diurnal Mean Thermal Structure

The diurnal mean temperature derived during the MY34 GDE (Ls = 204° on average) is shown in Figure 12. Compared to the situation described in Section 3.1, daily averaged temperatures have significantly increased (by +40–45 K) in the range 50°S–30°N, going from 180 to 185 K at Ls = 150°, p = 100 Pa to 220 K at Ls = 204°. At lower pressures, the temperature during the GDE is also very high (200 K at 10 Pa instead of 155–160 K a few months earlier). Elevated temperatures at $p < 50$ Pa are indeed a well-known characteristics of GDE (Kass et al., 2020). In addition, a branch of warm descending air is seen at high northern latitudes, with temperatures reaching 205–210 K on a daily average, located above a cold polar vortex in the lower atmosphere. We report a strong meridional gradient at altitudes below the 30 Pa level, with temperatures decreasing for instance from 220 K (100 Pa, 20°N) to 165 K (60°N). A more moderate equator-to-pole temperature gradient exists toward high southern latitudes, with temperatures still of 200 K at 70°S throughout the lower atmosphere. Temperatures simulated with the Mars PCM are in very good agreement with the observations except for a steeper meridional gradient in the modeled lower atmosphere. This corresponds to a ∼5 K too cold simulated polar vortex in the lower atmosphere, beyond 50°N and for $p > 100$ Pa.

Interestingly, several authors report that in the afternoon, the lower atmosphere (at 50 Pa) is warmer at mid-southern latitudes than at mid-northern ones during the GDE (Kass et al., 2020; Vlasov et al., 2022), linked with enhanced radiative forcing of the dust in the southern hemisphere (both due to the insolation at the current season, and the fact that there is more dust in the southern hemisphere during the peak of the storm). However, we see that on a diurnal mean basis, northern tropics are warmer than the southern ones at 50 Pa. This is consistent with the fact that the diurnal mean temperature also reflects warming from the circulation, namely the warm

descending branch located in the northern hemisphere. Unfortunately, due to the failing of the wave mode decomposition at $p < 10$ Pa south of 50°S (probably due to incorrect seasonal de-trending and hence, a subtle mix of seasonal and local time variations i.e., not fitted by our Equation 1), we cannot firmly conclude on the presence or not of a southern counterpart of this circulation branch in TIRVIM observations. However, given the excellent comparison with the model at other latitudes, we can reasonably rely on the behavior of the Mars PCM, which does not exhibit such a warm branch at high southern latitudes. In the simulation, the diurnal mean temperature is only moderately warmer at $p < 10$ Pa toward very high southern latitudes (south of 85°S, not shown). The diurnal mean temperature thus reflects primarily a solsticial-type circulation, with upwelling at high southern latitudes and downwelling at mid- and high- northern latitudes. This is consistent with the current season (Ls = 210°) and the rapid transition between the two-cell equinoxial-type circulation and the one-cell solsticial-type circulation.

4.2. Tide Characteristics

On top of the ∼40 K overall warming effect of the GDE at the diurnal mean scale at most latitudes (outside the cold polar vortex), very large tide amplitudes are observed during the storm. Before presenting the results, we briefly report on the detection of terdiurnal tide signatures below.

4.2.1. Extraction of the Terdiurnal Mode

Despite the rather limited local time coverage, we attempted to retrieve the amplitude and phase of the terdiurnal mode (TW3) during the GDE, hence amounting to a total of 7 parameters to fit instead of 5 in the previous case. This is motivated by the expected amplitudes of up to 4–5 K of this mode during dust storms, as noticed in the Mars PCM simulations. For some latitude bins and pressure levels, significantly better fits to the temperature data are indeed obtained with 7 instead of 5 parameters. Two of the best examples are shown in Figure 13 for the bins centered at 30°N near 5 Pa, and 30°S near 30 Pa (panels a and d). However, at high latitudes, the local time coverage is sometimes too sparse to confidently retrieve the tide parameters. For instance, fitting the terdiurnal tide parameters for the bin centered at 70°S leads to a better χ^2 (compared to fitting 5 parameters) but the reconstructed temperatures obtained with or without fitting TW3 are largely inconsistent at missing local times (see Figure 14). This figure illustrates well the degeneracy among different solutions. A similar behavior is noticed for the bins centered at 60°S and 60°N (although less extreme). For this reason, we proceed by running the decomposition method for both 5 and 7 parameters and keep the solution with a significantly better χ^2, except for the bins centered at 60°N, 60°S, and 70°S, where we choose to present results obtained with only 5 fitted parameters (DW1 and SW2 only). TW3 is only confidently constrained between 60°S and 40°N and ∼10 and 50 Pa, with derived amplitudes of 4–6 K. The fit to the high southern latitude data remains unsatisfactory for $p < 10$ Pa in any case, hence we will not interpret results in this region. Other examples of fits to the zonal mean temperature are shown in Figure 15.

4.2.2. Tide Amplitudes

We present the latitude-pressure cross-sections of the derived phase and amplitude for DW1, SW2, and TW3 in Figure 16. The main striking feature in the tide structure is a huge diurnal tide amplitude at high southern latitudes, reaching 35 K (hence, a peak-to-peak temperature variation of 70 K) at 60°S and 50 Pa. This is six to seven times higher than the tide amplitude derived at extra-tropical latitudes at Ls = 150°, a few months earlier. This amplitude is even larger than the value of 29 K reported by Kleinböhl et al. (2020) at 60°S from the 3 a.m.–3 p.m. temperature difference in MCS observations, which can be explained by the fact that temperature extrema occur near 6 a.m. and 6 p.m. (and not 3 a.m. and 3 p.m.), as can be seen in the fits to the data in Figure 15, panel a. Our derived amplitude is also significantly greater than the peak amplitude of 20–22 K reported by Guzewich et al. (2014) from TES limb measurements obtained at 2 a.m. and 2 p.m. during the 2001 GDE. In the northern hemisphere, another local maximum is present in DW1, reaching 17 K at 45°N. This is close to the 15 K amplitude reported near 50°N, 50 Pa by Kleinböhl et al. (2020) from MCS observations. Diurnal tide amplitudes are minimal and amount to 2–6 K in a narrow region centered at 20°N in the lower atmosphere, and over a broader area (30°S–40°N) in the middle atmosphere, for $p < 50$ Pa. This pattern is very different from the pre-storm season, where the diurnal tide amplitude is known to be strong both near 50° latitude and the equator. This is consistent with the weakening of the diurnal tide at the equator during GDE as documented by Guzewich et al. (2014) and Kleinböhl et al. (2013), although here we are able to better characterize the tide's absolute amplitude and separate it from the contribution of the terdiurnal tide.

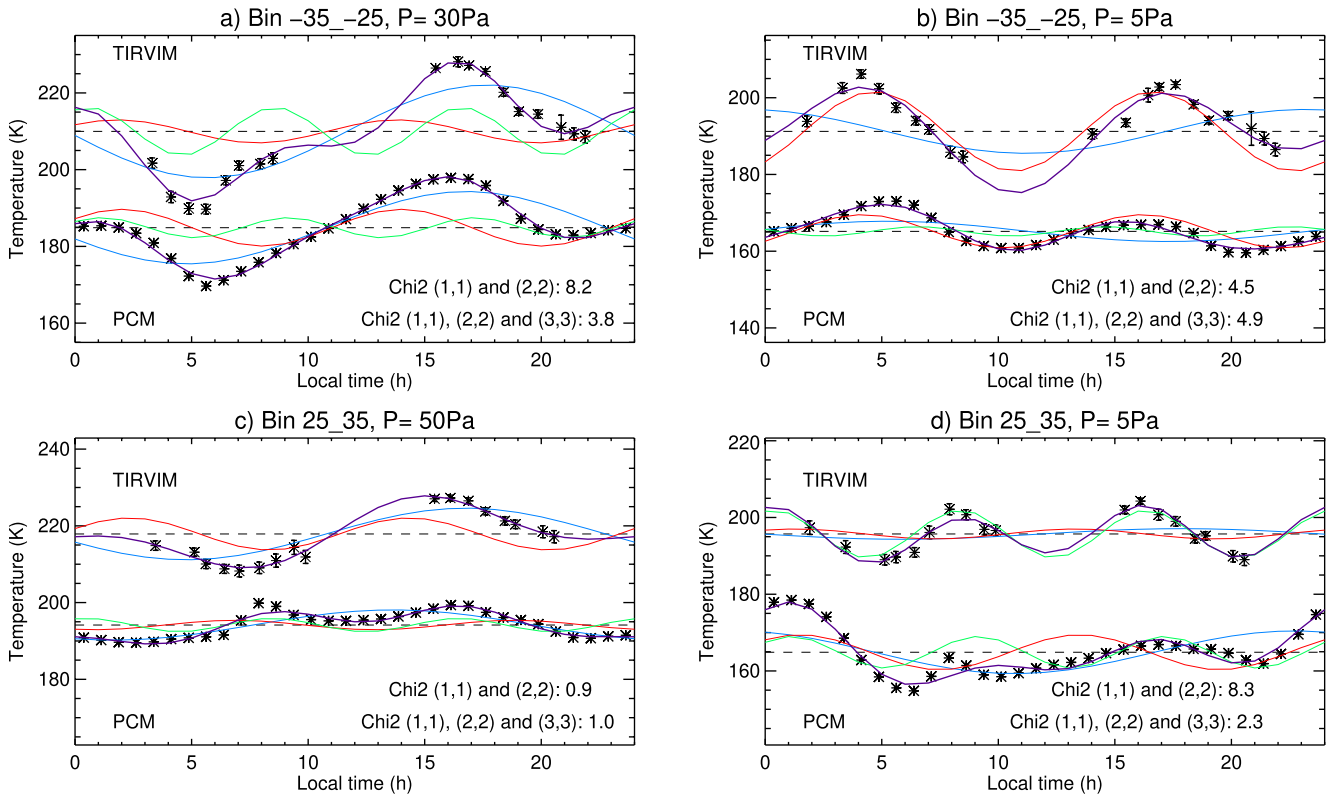

Figure 13. Examples of tide decomposition during the global dust event for several latitude bins and pressure levels, as labeled. The zonally averaged temperatures as measured by TIRVIM, as a function of local time, are shown as black stars. The fitted diurnal mean temperature is shown as a horizontal dashed line while the colored lines represent the fitted contributions from the diurnal (in blue), semidiurnal (in red) and terdiurnal (in green, when applicable) modes. The sum of these contributions (best fits to the data) is shown in purple. In addition to TIRVIM observations, we display the Mars Planetary Climate Model tide decomposition, shifted by −25 K. Values of the χ^2 corresponding to TIRVIM observations are also given, with and without fitting the terdiurnal mode.

The semidiurnal tide also exhibits a very different pattern compared to the pre-storm season. Instead of being maximum at the equator, we find three localized regions of high amplitude. We report a first local maximum in the lower atmosphere near 100 Pa, where SW2 reaches an amplitude of 12 K at latitude 20–40°S, while its amplitude is negligible in the opposite hemisphere. The SW2 signature is thus highly asymmetric between the two hemispheres at this pressure level. Second, for $p < 10$ Pa, we report two local maxima: one near 30–50°S (reaching 12 K, hence twice as strong as the diurnal tide amplitude at this latitude and pressure level) and another one near 40–60°N (reaching 8 K, commensurate to the diurnal tide there). Despite the lower sensitivity of TIRVIM at these lower pressure levels, the signature of the semidiurnal tide is very clear in the data (see fits for the case 30°S, 5 Pa in Figure 13b and for 50°N, 5 Pa in Figure 15d). In this pressure range ($p < 10$ Pa) the structure of the SW2 component is more symmetric with respect to the equator. Modeling studies have suggested that during a GDE, the semidiurnal tide amplitude would rise significantly as a result of a larger quantity of dust over a broad altitude range (Forbes & Miyahara, 2006; Wilson & Richardson, 2000). Data assimilation of TES nadir observations during the MY25 global storm (Wilson et al., 2007) yielded an amplitude of ~6 K for the equatorial SW2 component (expressed as a temperature measured at 15 μm, representative of the 50 Pa level), which is commensurate to our derived SW2 amplitude. According to this data assimilation, SW2 featured another local maximum (6 K as well) near 60°S during the MY25

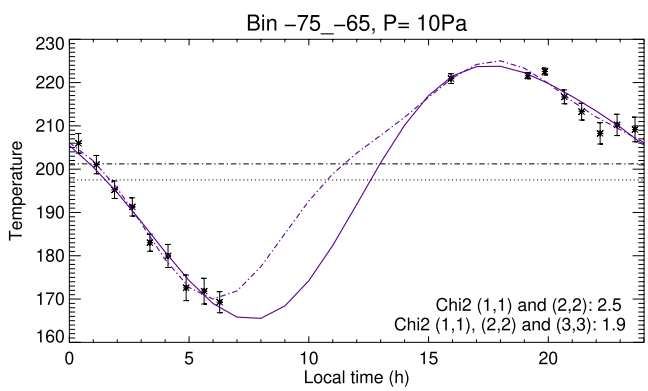

Figure 14. Zonally averaged temperature as a function of local time as measured by TIRVIM (black stars) during the GDE, for the bin centered at 70°S and $p = 10$ Pa. Best fits to the data are shown in purple with only the DW1 and SW2 modes (solid line) or including the TW3 mode (dot-dashed line). The fitted diurnal mean temperature is shown as horizontal dot-dashed or dotted lines whether the TW3 mode was included or not. This case illustrates the worst example of the degeneracy in fitting tide parameters, due to a large gap in local time coverage.

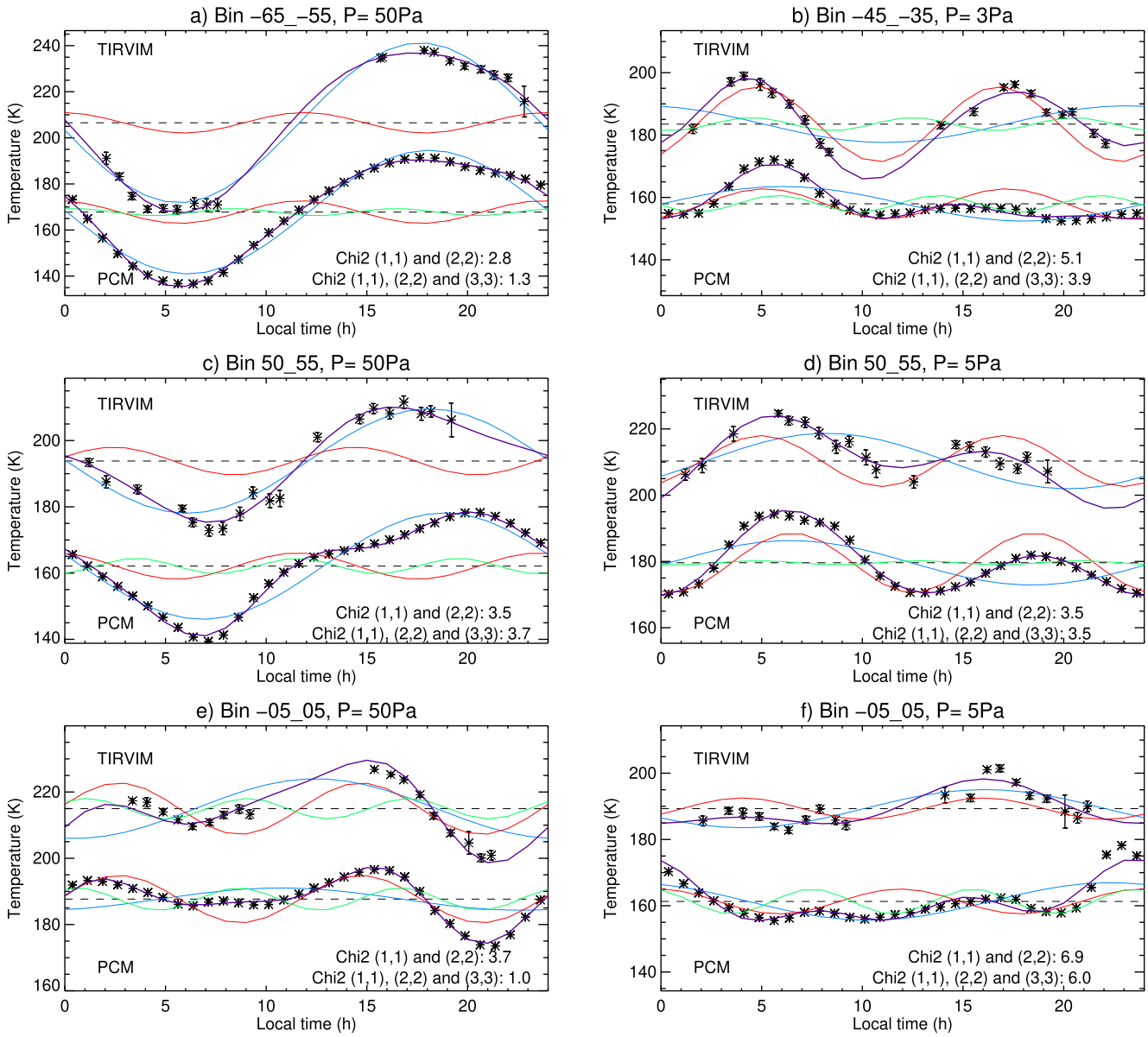

Figure 15. Same as Figure 13 for other latitude bins and pressure levels. Results from the Mars Planetary Climate Model were shifted by −25 K except for the bin 60°S, 50 Pa (shift of −50 K) and the bin 50N, 50 Pa (shift of −40 K).

global dust storm, while here we report a local maximum near 30°S. This difference might be caused by different dust distributions among the storms.

The terdiurnal tide amplitude is more difficult to assess given its lower amplitude (on top of higher amplitude signals from the other two modes) and the limited local time coverage. However, we can clearly assess its detection and relatively high amplitudes, reaching 5–6 K, in two distinct regions. The first maximum extends from 10 to 60°S and 15–50 Pa (roughly an altitude range in between the two SW2 local maxima at 30–40°S); the second one is found near 20–40°N for $p < 10$ Pa (slightly to the south of a SW2 local maxima). Including the terdiurnal mode in these cases lead to a significant χ^2 reduction, by a factor of 2–3 (see Figure 13). Interestingly, these maxima are located where the SW2 amplitude is found minimum. Amplitude of TW3 of typically 0.5 K were reported during the aphelion season by Fan, Forget, et al. (2022) but to our knowledge, there is no previous observational study of TW3 during dust storms.

We estimate the error on tide amplitudes to be of the order of 2 K, reaching 3–4 K at high latitudes, based on measurement error, on incomplete diurnal coverage and on imperfect "seasonal" de-trending. Similarly to the Ls = 150° case, the tide amplitudes are expected to vary over the course of the 25-sols period considered here, as

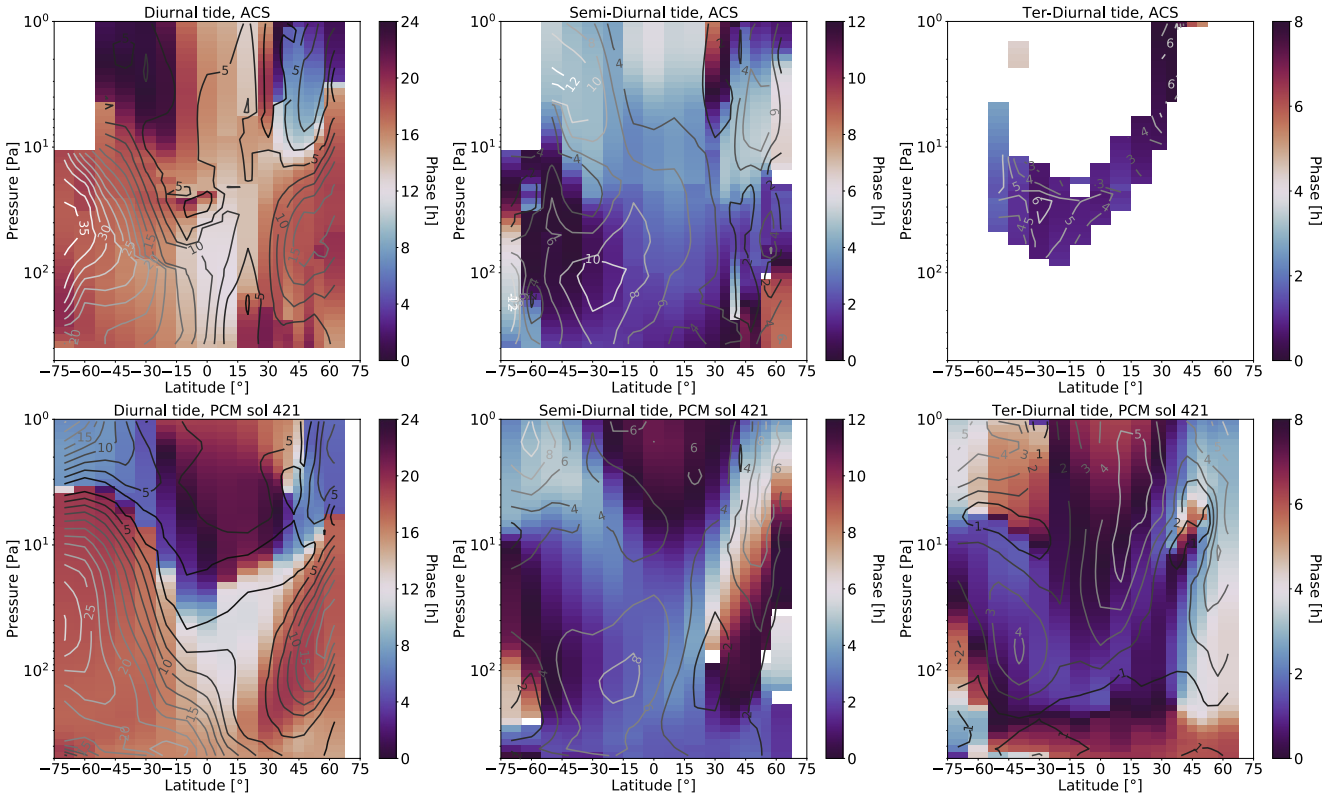

Figure 16. Phase (color, in hours) and amplitude (contours, in Kelvin) of the diurnal (left), semidiurnal (middle) and terdiurnal (right) migrating tide derived from Atmospheric Chemistry Suite/TIRVIM (upper row) or from the Mars Planetary Climate Model (bottom row) during the global dust event of MY34, at sol 421 (Ls = 208°). Gaps in the terdiurnal mode amplitude correspond to cases where the fit to the data was not improved when TW3 was included.

the storm is evolving. For instance, in the Mars PCM, changes in amplitude of typically 2 K are evident between sol 412 and sol 422 (Ls = 204–209°). We can assume that this variability is representative of reality and hence impacts our sensitivity.

Comparisons to tide characteristics extracted from the Mars PCM simulations are shown in the bottom row of Figure 16 as well as in the fits examples (Figures 13 and 15). Note here that we did not attempt to extract the model temperature profiles at TIRVIM exact latitude, longitude, local time and date, due to the sparser local time coverage and to avoid the potential effects of imperfect representation of the evolution of the dust storm over the 25-sols period in the model. Rather, we present tide parameters extracted for one representative Martian sol number 421 (Ls = 208°).

Overall, we find that the model reproduces very well the structure of DW1 during the GDE: the location and amplitude of the two extrema qualitatively match the observations, although we report a tide amplitude 8 K greater at high southern latitudes compared to the Mars PCM (even without applying a vertical smoothing). The fact that the tide minimum amplitude is located near 20°N (and not at the equator) in the lower troposphere is also well reproduced. The amplitude of DW1 is found minimum (only 2 K) near 30 Pa at the equator, which is consistent with the weakening of the gravest Hough mode of the diurnal tide due to increased dust loading in the simulations by Wilson and Richardson (2000). The structure of SW2 in the Mars PCM also features striking similarities to our observations, in particular with the display of a strong north-south asymmetry in the lower atmosphere. Indeed, the SW2 amplitude reaches 8 K in the model at 20°S and 100 Pa while it is minimum (less than 1 K) at 20–30°N. The main difference is that the latitude of these extrema are located ∼10° closer to the equator than in the observations. In the upper part of the atmosphere, SW2 is found maximum near 50°N and 50°S in the Mars PCM, which qualitatively matches our findings, although in the observations, the southern maximum is more extended in pressure and latitude: its amplitude is greater than 5 K in the region 25–50°S and $p < 10$ Pa, while it is restricted to 40–50°S and $p < 3$ Pa in the model.

We also report an overall model-observation agreement for TW3. Indeed, terdiurnal tide amplitudes simulated with the Mars PCM feature a 4 K local maximum near 40°S and 50 Pa that matches the location of a corresponding

extremum in TIRVIM observations. The simulated amplitudes are the strongest between 0° and 20°N for pressures less than 30 Pa, where they reach 4–5 K. There is apparently no such broad low-latitude maximum in the observations, but a similarly high TW3 amplitude region is found around 30°N at pressures below 10 Pa in the observations, which could correspond to the structure seen in the model, but shifted toward the northern tropics for unknown reasons.

4.2.3. Tide Phases and Vertical Structure

The phase structure of DW1 is found to differ completely from the pre-storm season. For $p > 10$ Pa, DW1 is now indeed dominated by the extra-tropical vertically trapped Hough modes that are excited by strong dust radiative forcing, and that had a small influence at Ls = 150°. In this pressure range, the phase of DW1 is locked at 5–6 p.m. through a large part of the extra-tropical atmosphere: up to 5–10 Pa at 30–60°S and up to 10–20 Pa at 30–60°N. This slight hemispheric asymmetry in the altitude range where DW1 is vertically trapped is consistent with the expectation that the extratropical tide responds to local heating by dust, which extends higher in the southern hemisphere during the MY34 storm (Kleinböhl et al., 2020). A similar phase behavior was reported by Wu et al. (2021) from MCS data during the MY33 dusty season, and is also well reproduced by the Mars PCM or other previous modeling studies (Banfield et al., 2003; Wilson & Richardson, 2000). The vertically propagating equatorial (1,1) Hough mode is clearly attenuated; rather, the equatorial region is strongly influenced by the extra-tropical modes. To further illustrate the meridional structure of the tide's phases, we show in Figure 17 the diurnal evolution of the reconstructed temperature field with latitude at a pressure of 50 Pa, from TIRVIM data and from the Mars PCM, along with the reconstructed signals from the diurnal and semidiurnal tides. The left panels of this figure compare quite well with the ones presented in Wilson and Richardson (1999), showing the diurnal evolution of the T_{15} temperature simulated and measured by the Viking mission during the 1977 storms. A similar figure for the Ls = 150° case is presented in Figure 18. Note that the 6 p.m. phase of DW1 at high latitudes is similar at Ls = 150° or during the GDE: the storm does not impact the timing of the extrema but reinforces their amplitude. Rather, at the equator, the DW1 phase during the GDE (e.g., noon at 50 Pa) is intermediate between the pre-storm one (6 a.m. at 50 Pa at Ls = 150°) and the high-latitude one. A similar phase structure is predicted by the Mars PCM for $p > 10$ Pa.

At lower pressures, we report abrupt phase changes at mid-latitudes during the GDE, but with opposite behavior in the two hemispheres. At 40–60°N, the phase rapidly shifts from 6 p.m. for $p > 10$ Pa toward earlier local times of 6–8 a.m. for $p < 10$ Pa. On the other hand at 20–60°S, the phase changes more gradually from 5 to 6 p.m. ($p > 10$ Pa) to later local times, reaching midnight at $p = 2$ Pa, that is, corresponding to an upward-propagating phase (see Figure 19). Abrupt phase shifts are also predicted by the Mars PCM at mid-latitudes and follow quite well the observed ones up to $p = 5$ Pa. At even lower pressures, the phase at 40°S suddenly changes to 6 a.m. in the Mars PCM, which does not match the observations, while the phase at mid-northern latitudes starts to increase toward later local times (see Figure 19). Retrieving correctly abrupt phase changes from nadir observations is challenging in this pressure range, as TIRVIM information content quickly decreases for $p < 10$ Pa and has a broader contribution function, leading to an underestimation of the tide's amplitudes. The smaller the tide amplitude, the more difficult it is to assess its phase, especially given the uneven local time sampling. However, some model-observation mismatches appear quite robust when looking at the fits to the data. For instance at 40°S and 3 Pa, the amplitude of SW2 is almost three times greater in the observations than in the PCM, with temperature maxima at 4 a.m. and 4 p.m. of similar amplitude (see panel b of Figure 15). If the phase of DW1 was indeed at 6 a.m. (as predicted by the PCM), the 4 p.m. temperature maximum corresponding to SW2 would be compensated by the temperature minimum of DW1 at 6 p.m., which is not the case. In addition, we recall that our a priori temperature profile does not contain information on the phase (it is the same at all local times) so that our retrievals are not biased in that respect. Hence, the phase signatures reported at $p < 10$ Pa look rather robust.

The different phase characteristics between the northern and southern hemispheres might be related to the different vertical distribution of water ice clouds at 40–60°S and 40–60°N. Indeed, Wu et al. (2021) also found examples of upward phase propagation of the diurnal tide from 10 to 1 Pa in the southern hemisphere during major regional dust storms. The authors linked this behavior to the thermo-tidal forcing by high altitude (~1 Pa) water ice clouds. Our results at least partly support this theory, as elevated water ice clouds were also reported during the MY34 GDE (Stcherbinine et al., 2020). The elevated SW2 amplitude that we derive from TIRVIM at high altitudes also supports a significant forcing by water ice clouds, which could be underestimated in the Mars PCM due to unrealistic water ice properties (particle sizes for instance) and/or spatial distribution. However, elevated clouds

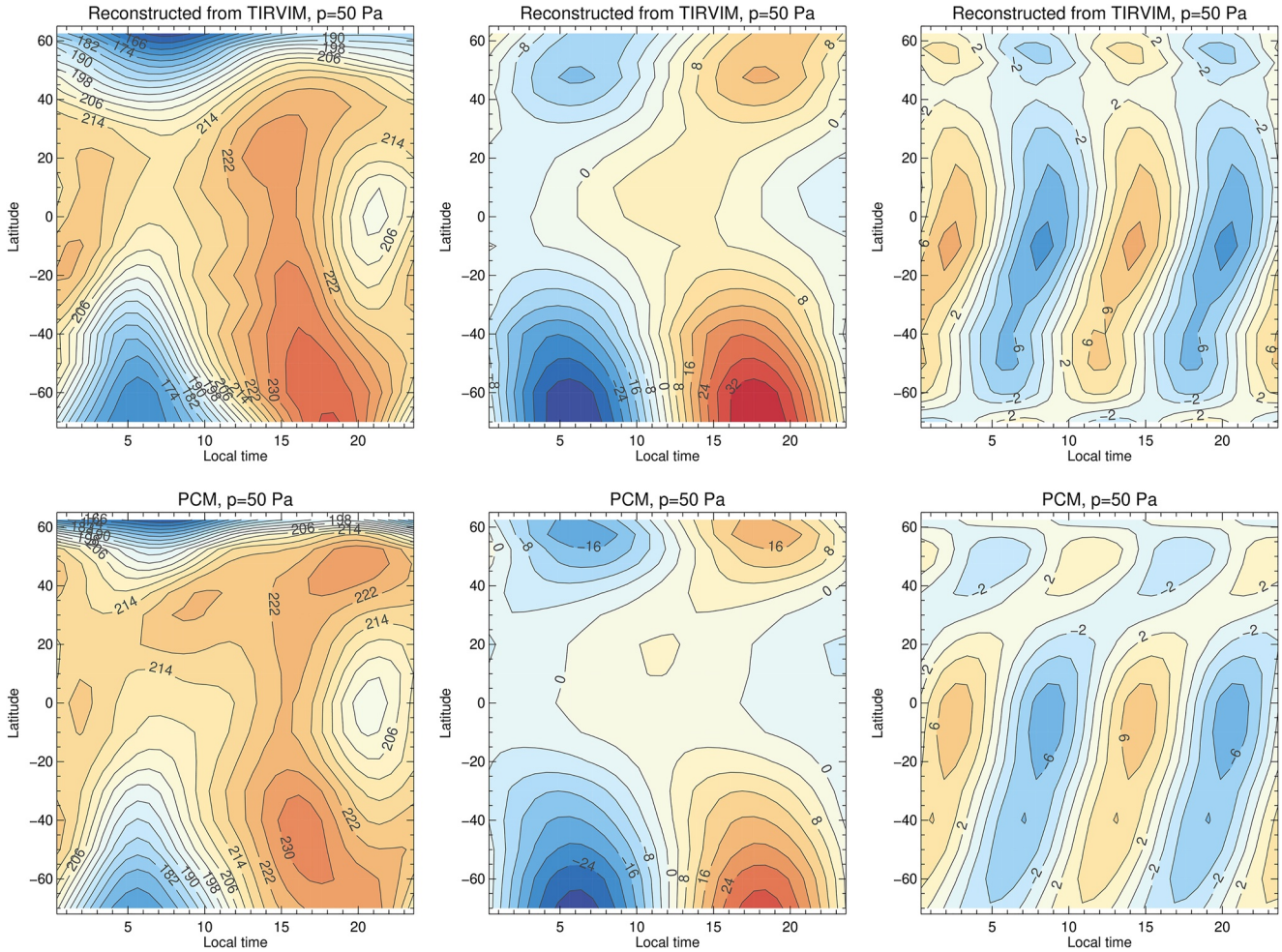

Figure 17. Left: Diurnal variation of the temperature at $p = 50$ Pa reconstructed from fitting TIRVIM data (top) or from the Mars Planetary Climate Model (bottom) during the global dust event of MY34. The middle and right panels show the reconstructed diurnal and semidiurnal modes, respectively.

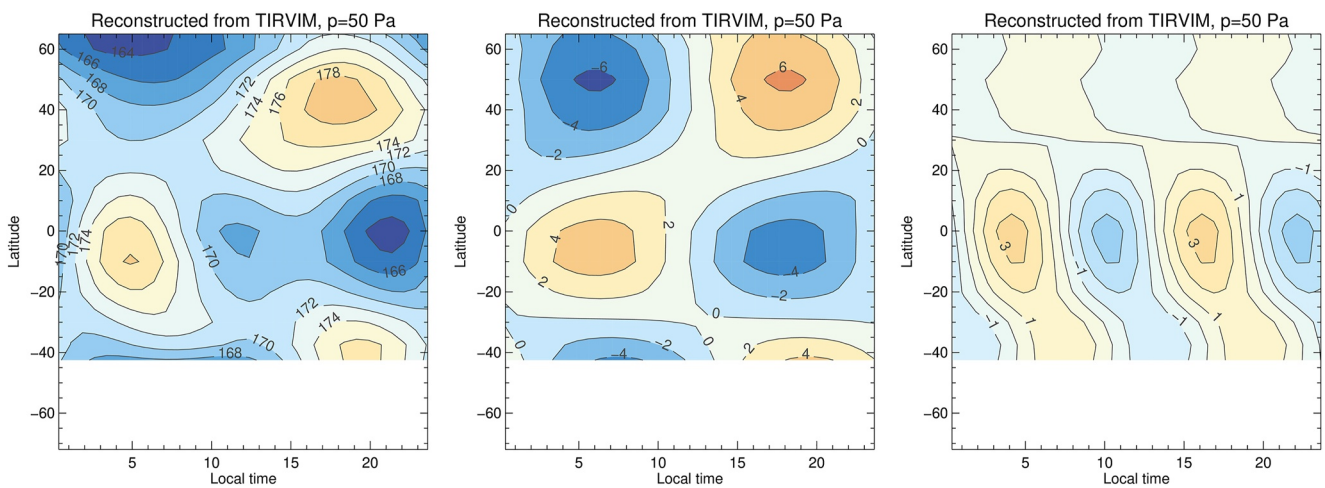

Figure 18. Same as Figure 17, but reconstructed from TIRVIM observations at Ls = 150°.

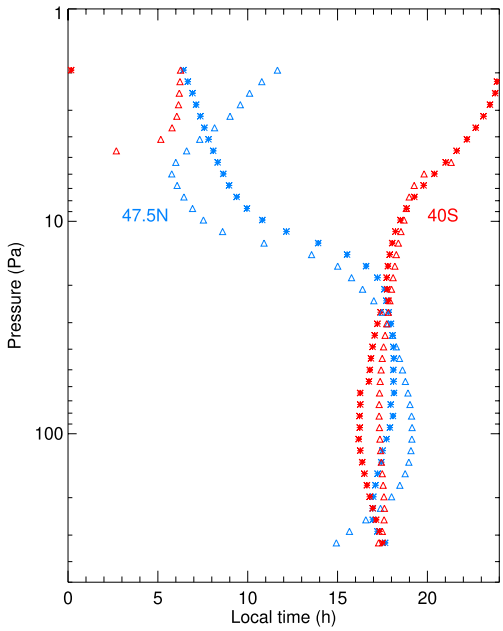

Figure 19. Phase of the diurnal tide with pressure at 40°S (red) and 47.5°N (blue) during the MY34 GDE (Ls ~ 200°) as derived from Atmospheric Chemistry Suite/TIRVIM (stars) and as predicted by the Mars Planetary Climate Model (triangles).

were apparently present in similar amounts in the southern and northern hemisphere during the MY34 GDE (Liuzzi et al., 2020), so that this does not fully explain why only mid-southern latitudes exhibit an upward-propagating phase behavior. The quantitative impact of these forcings on the tides' phase structure remains to be further investigated in future studies. Note that data assimilation of TIRVIM temperature and dust retrievals in the Mars PCM does not produce an upward-propagating phase at southern mid-latitudes (see Figure 19 in Young et al., 2022): this might be because about half of TIRVIM vertical profiles were not included in the assimilation for $p < 5$ Pa (due to their lower information content). An assimilation including water ice cloud observations would also further improve the analysis. Finally, we also report a different phase structure for DW1 between the observations and the model in the equatorial region for $p < 30$ Pa: in the observations, the phase does not vary much with altitude (it stays in the range noon-3 p.m. throughout the atmosphere) while the phase varies a lot and reaches 9 p.m. at $p = 5$ Pa in the Mars PCM. Data assimilation of TIRVIM observations does yield a significant phase change in the analysis compared to the PCM simulations (Young et al., 2022), but the physical reasons behind this observation-model mismatch in phase remains unknown.

Regarding the semidiurnal tide, we find that the temperature peaks at ~3 a.m. near the equator (4 a.m. before the storm) in the lower atmosphere. This is in excellent agreement with the tidal model experiments made by Wilson and Richardson (2000), in the case of a high atmospheric dust content, and with the observations by the Viking Infrared Thermal Mapper during the 1977b storm discussed by the authors. The SW2 phase vertical and meridional structure reported from TIRVIM is similar to the one predicted by the Mars PCM except in two regions: (a) at low latitudes and $p < 10$ Pa, where we derive a phase of 6 a.m. instead of noon in the Mars PCM; and (b) at northern mid-latitudes between 10 and 100 Pa, where there is also a 6 hr out-of-phase difference between TIRVIM and the PCM. Note that these observation-model mismatches occur where the amplitude of SW2 is rather low (2–4 K), making the phase determination challenging from the observations. However, looking at the data directly (see Figure 13), it is clear that the diurnal evolution of the temperature at 30°N, 50 Pa is not well captured by the Mars PCM: instead of featuring a local minimum near 8 a.m., the model predicts a local temperature maximum at this time of the day. Another striking disagreement is displayed for the bin 30°N at 5 Pa, where diurnal variations in TIRVIM are clearly dominated by the terdiurnal tide while in the Mars PCM, DW1, SW2, and TW3 contribute almost equally. It is also worth noting that the model-observation mismatches in phase and amplitude north of 30°N occur where the latitudinal temperature gradient also disagree at the diurnal mean scale. According to Wu et al. (2017), differences in meridional gradient, hence of vertical shear of the zonal wind, could impact the vertical propagation of waves, hence the tides's phases. Other potential sources of observation-model mismatch are an incorrect vertical distribution of aerosol (dust and water ice clouds), or incorrect representation of wave forcings such as gravity waves.

Figure 17 highlights that the SW2 phase drifts slowly earlier in the day at higher latitudes, with peaks occurring near noon and midnight at 60°S and 60°N. This behavior was not present before the storm (see Figure 18). A similar phase tilt is seen in the Mars PCM at 50 Pa in the southern hemisphere. Such a shift implies that asymmetric Hough modes contribute significantly to the semidiurnal tide pattern. Indeed, if the gravest Hough function (equatorially symmetric) was the only contributor, there would be no phase shift with latitude. Interestingly, such a phase tilt was reported among the surface pressure measurements made by the Viking landers at 22°N and 48°N during the 1977 storms and has been successfully explained assuming asymmetric thermotidal forcing between the two hemispheres, namely an asymmetric dust distribution (Bridger & Murphy, 1998). As there was indeed more dust in the southern hemisphere during the MY34 GDE, this characteristics is certainly the reason behind the hemispheric asymmetry of the SW2 mode and its phase tilt with latitude.

5. Conclusion

In this paper, we reported on the migrating tide amplitudes and phases derived from the analysis of vertical temperature profiles, themselves retrieved from the TIRVIM-ACS instrument onboard the ExoMars TGO in April–July 2018, before and during the MY34 GDE. The strength of the TIRVIM observations is to cover a great variety of local times, although a complete coverage of diurnal cycle takes 54 sols, mixing to a certain extent seasonal with diurnal variations. To make the most out of TIRVIM observations, we used contemporaneous temperature profiles from the MCS limb sounder to seasonally de-trend TIRVIM temperatures. We have shown that this improved the derived semidiurnal tide amplitudes and phases. We summarize below the main findings on tide characteristics at the two considered seasons.

At Ls = 150°, the latitude/pressure structure of the migrating tides captured by TIRVIM are in excellent agreement with that predicted from tidal theory. DW1 is dominated by the gravest (1,1) Hough function, with vertically propagating tides at the equator, a minimum amplitude near 30°, and again a downward phase propagation near 50° latitude corresponding to the negative lobes of the (1,1) Hough function: the vertically trapped modes that are expected to dominate at high latitudes do not seem to influence the mid-latitudes at this season. The derived amplitudes, of typically 4–5 K at the equator for the diurnal mode, and 2–4 K for the semidiurnal mode, are very similar to that obtained from the Mars PCM once TIRVIM averaging kernels are applied to the modeled profiles. The main features of the migrating tides are well reproduced in the PCM, including the slight off-equatorial maximum amplitudes observed at 5–10°S at this season. Vertical wavelengths at the equator are similar in both the model and the observations, with values of 4.4 scale heights (H) for the diurnal tide and 7.3 H for the semidiurnal tide at the equator. This suggests that the thermotidal forcing in our general circulation model and the atmospheric response to it is realistic. The only significant disagreement found is a small (1 hr and a half) phase shift of the diurnal mode, with temperature extrema occurring too late in the model. This was already reported by Fan, Guerlet, et al. (2022) and Fan, Forget, et al. (2022) at Ls = 90° and remains to be explained. Differences in the vertical, meridional or zonal distribution of aerosols between model and observations could play a role in this phase shift, as well as interferences with non-migrating tides (eastward-propagating Kelvin modes).

During the MY34 GDE, we report strong amplitudes of the diurnal tide near 60°S and 50°N, being maximum near 50 Pa and amounting to 35 and 17 K, respectively, and being vertically trapped up to 20–5 Pa. Thanks to TIRVIM we can more clearly assess the phase of tides during the GDE, with a temperature maximum occurring near 6 p.m. for the mid and high latitude observations up to ∼20 Pa, which is similar to that before the storm at these high latitudes and this pressure level. On the other hand, the amplitude of the diurnal mode at the equator has remain similar (for $p > 50$ Pa) or smaller (for $p < 50$ Pa) compared to that before the storm, in agreement with the predictions that the gravest (1,1) Hough function is weakened by significant dust loading (Wilson & Richardson, 2000). The amplitude of the SW2 mode is increased during the storm, reaching 8–12 K at $p = 1$–10 Pa and $p = 70$–300 Pa. However, these high amplitudes are well offset from the equator and are located near 20–30°S. We assess for the first time in the temperature field the phase of the SW2 mode during a GDE, which corresponds to maxima near 3 a.m. and 3 p.m. near the equator, with a phase tilt with latitude (earlier maxima at high latitudes). This characteristics is consistent with the tidal model experiments of Bridger and Murphy (1998), in which a hemispheric asymmetry in dust distribution increases the importance of the asymmetric Hough functions and results in a meridional phase tilt in the surface pressure signature of SW2. We also report hints of upward-propagating phase of the diurnal tide at mid-southern latitudes for $p < 10$ Pa, which remains to be further investigated and might be linked to a thermo-tidal forcing by elevated water ice clouds (Wu et al., 2021). Finally, we detected for the first time signals of the terdiurnal tide during the storm, amounting to 6 K near 30°S, 20–50 Pa and near 30°N, 1–10 Pa. Most of these characteristics are qualitatively consistent with the Mars PCM run with the dust scenario for MY34 (i.e., with dust column values imposed to match that observed from the MCS during that year, with a simple linear interpolation between two successive sols to represent diurnal variations). Minor model-observations disagreements are noticed regarding the tides characteristics and the diurnal mean thermal structure that reflect slight differences in the strength of the Hadley circulation and in the location of the edge of the polar vortex, hence on the conditions for vertical propagation of the waves. The vertical distribution of dust and water ice clouds, and its diurnal variation, are also known to be imperfect in the Mars PCM, which could also explain the model-observation mismatches. However, these disagreements remain small, implying that with correct thermo-tidal forcing (to first order), our model reproduces well the response of the atmosphere to high dust contents. It will be interesting to investigate in the future the characteristics of the non-migrating tides

during the GDE. This might be challenging from TIRVIM observations due to their rather limited local time coverage (two times 6 hours in the period considered in this paper), but other instruments with denser local time coverage such as EMIRS onboard EMM might witness another GDE and shed more light on these phenomena. Data assimilation of several datasets (temperature, dust, water ice; from nadir and limb sounders) should also be developed to better constrain the tide's characteristics without being hampered by the mix of secular trends and diurnal variations inherent to TIRVIM observational scheme.

Data Availability Statement

Mars Climate Sounder data are publicly available on the Atmospheres Node of NASA's Planetary Data System (McCleese, 2008), also accessible at this link: MCS (https://atmos.nmsu.edu/data_and_services/atmospheres_data/MARS/mcs.html). The TIRVIM temperature retrievals used in this paper are available in NetCDF format on the Institut Pierre Simon Laplace (IPSL) data server (Guerlet, 2021).

Acknowledgments
ExoMars is a space mission of ESA and Roscosmos. The ACS experiment is led by IKI, the Space Research Institute in Moscow, assisted by LATMOS in France. This work, exploiting ACS/TIRVIM data, acknowledges funding by CNES. The science operations of ACS are funded by Roscosmos and ESA. ACS/TIRVIM team at IKI acknowledges the subsidy of the Ministry of Science and High Education of Russia. Simulations with the Mars PCM used in this article were performed using HPC computing resources from GENCI-CINES (Grant 2022-A0120110391). Armin Kleinböhl acknowledges support from NASA's Mars Data Analysis program (80NM0018F0719). Work at the Jet Propulsion Laboratory, California Institute of Technology, is performed under contract with the National Aeronautics and Space Administration. We thank John Wilson and an anonymous referee for their constructive comments that helped improve the contents of this manuscript.

References

Banfield, D., Conrath, B., Pearl, J. C., Smith, M. D., & Christensen, P. (2000). Thermal tides and stationary waves on Mars as revealed by Mars Global Surveyor thermal emission spectrometer. *Journal of Geophysical Research*, *105*(E4), 9521–9538. https://doi.org/10.1029/1999JE001161

Banfield, D., Conrath, B. J., Smith, M. D., Christensen, P. R., & Wilson, R. J. (2003). Forced waves in the Martian atmosphere from MGS TES nadir data. *Icarus*, *161*(2), 319–345. https://doi.org/10.1016/S0019-1035(02)00044-1

Bridger, A. F. C., & Murphy, J. R. (1998). Mars' surface pressure tides and their behavior during global dust storms. *Journal of Geophysical Research*, *103*(E4), 8587–8602. https://doi.org/10.1029/98JE00242

Fan, S., Forget, F., Smith, M. D., Guerlet, S., Badri, K. M., Atwood, S. A., et al. (2022). Migrating thermal tides in the Martian atmosphere during aphelion season observed by EMM/EMIRS. *Geophysical Research Letters*, *49*(18), e99494. https://doi.org/10.1029/2022GL099494

Fan, S., Guerlet, S., Forget, F., Bierjon, A., Millour, E., Ignatiev, N., et al. (2022). Thermal tides in the Martian atmosphere near northern summer solstice observed by ACS/TIRVIM onboard TGO. *Geophysical Research Letters*, *49*(7), e97130. https://doi.org/10.1029/2021GL097130

Forbes, J. M. (1995). Tidal and planetary waves. *Geophysical Monograph Series*, *87*, 67–87. https://doi.org/10.1029/GM087p0067

Forbes, J. M., & Miyahara, S. (2006). Solar semidiurnal tide in the dusty atmosphere of Mars. *Journal of the Atmospheric Sciences*, *63*(7), 1798–1817. https://doi.org/10.1175/JAS3718.1

Forbes, J. M., Zhang, X., Forget, F., Millour, E., & Kleinböhl, A. (2020). Solar tides in the middle and upper atmosphere of Mars. *Journal of Geophysical Research: Space Physics*, *125*(9), e28140. https://doi.org/10.1029/2020JA028140

Forget, F., Hourdin, F., Fournier, R., Hourdin, C., Talagrand, O., Collins, M., et al. (1999). Improved general circulation models of the Martian atmosphere from the surface to above 80 km. *Journal of Geophysical Research*, *104*(E10), 24155–24176. https://doi.org/10.1029/1999JE001025

Guerlet, S. (2021). ACS/TIRVIM temperature and aerosol retrievals [Dataset]. ESPRI/IPSL. https://doi.org/10.14768/AB765EBA-0C1D-47B6-97D6-6390C63F0197

Guerlet, S., Ignatiev, N., Forget, F., Fouchet, T., Vlasov, P., Bergeron, G., et al. (2022). Thermal structure and aerosols in Mars' atmosphere from TIRVIM/ACS onboard the ExoMars trace gas orbiter: Validation of the retrieval algorithm. *Journal of Geophysical Research: Planets*, *127*(2), e07062. https://doi.org/10.1029/2021JE007062

Guzewich, S. D., Talaat, E. R., & Waugh, D. W. (2012). Observations of planetary waves and nonmigrating tides by the Mars Climate Sounder. *Journal of Geophysical Research*, *117*(E3), E03010. https://doi.org/10.1029/2011JE003924

Guzewich, S. D., Wilson, R. J., McConnochie, T. H., Toigo, A. D., Banfield, D. J., & Smith, M. D. (2014). Thermal tides during the 2001 Martian global-scale dust storm. *Journal of Geophysical Research: Planets*, *119*(3), 506–519. https://doi.org/10.1002/2013JE004502

Haberle, R. M., Kahre, M. A., Hollingsworth, J. L., Montmessin, F., Wilson, R. J., Urata, R. A., et al. (2019). Documentation of the NASA/Ames Legacy Mars global climate model: Simulations of the present seasonal water cycle. *Icarus*, *333*, 130–164. https://doi.org/10.1016/j.icarus.2019.03.026

Kass, D. M., Schofield, J. T., Kleinböhl, A., McCleese, D. J., Heavens, N. G., Shirley, J. H., & Steele, L. J. (2020). Mars climate sounder observation of Mars' 2018 global dust storm. *Geophysical Research Letters*, *47*(23), e83931. https://doi.org/10.1029/2019GL083931

Kleinböhl, A., Schofield, J. T., Kass, D. M., Abdou, W. A., Backus, C. R., Sen, B., et al. (2009). Mars Climate Sounder limb profile retrieval of atmospheric temperature, pressure, and dust and water ice opacity. *Journal of Geophysical Research*, *114*(E10), E10006. https://doi.org/10.1029/2009JE003358

Kleinböhl, A., Spiga, A., Kass, D. M., Shirley, J. H., Millour, E., Montabone, L., & Forget, F. (2020). Diurnal variations of dust during the 2018 global dust storm observed by the Mars climate sounder. *Journal of Geophysical Research: Planets*, *125*(1), e06115. https://doi.org/10.1029/2019JE006115

Kleinböhl, A., Wilson, J. R., Kass, D., Schofield, J. T., & McCleese, D. J. (2013). The semidiurnal tide in the middle atmosphere of Mars. *Geophysical Research Letters*, *40*(10), 1952–1959. https://doi.org/10.1002/grl.50497

Korablev, O., Montmessin, F., Trokhimovskiy, A., Fedorova, A. A., Shakun, A. V., Grigoriev, A. V., et al. (2018). The Atmospheric Chemistry Suite (ACS) of three spectrometers for the ExoMars 2016 trace gas orbiter. *Space Science Reviews*, *214*(1), 7. https://doi.org/10.1007/s11214-017-0437-6

Lee, C., Lawson, W. G., Richardson, M. I., Heavens, N. G., Kleinböhl, A., Banfield, D., et al. (2009). Thermal tides in the Martian middle atmosphere as seen by the Mars climate sounder. *Journal of Geophysical Research*, *114*(E3), E03005. https://doi.org/10.1029/2008JE003285

Leovy, C. B., & Zurek, R. W. (1979). Thermal tides and Martian dust storms: Direct evidence for coupling. *Journal of Geophysical Research*, *84*(B6), 2956–2968. https://doi.org/10.1029/JB084iB06p02956

Lindzen, R. S. (1970). The application and applicability of terrestrial atmospheric tidal theory to Venus and Mars. *Journal of the Atmospheric Sciences*, *27*(4), 536–549. https://doi.org/10.1175/1520-0469(1970)027<0536:TAAAOT>2.0.CO;2

Lindzen, R. S., & Chapman, S. (1969). Atmospheric tides. *Space Science Reviews*, *10*(1), 3–188. https://doi.org/10.1007/BF00171584

Liuzzi, G., Villanueva, G. L., Crismani, M. M. J., Smith, M. D., Mumma, M. J., Daerden, F., et al. (2020). Strong variability of Martian water ice clouds during dust storms revealed from ExoMars trace gas orbiter/NOMAD. *Journal of Geophysical Research: Planets*, *125*(4), e06250. https://doi.org/10.1029/2019JE006250

Lo, D. Y., Yelle, R. V., Schneider, N. M., Jain, S. K., Stewart, A. I. F., England, S. L., et al. (2015). Nonmigrating tides in the Martian atmosphere as observed by MAVEN IUVS. *Geophysical Research Letters*, *42*(21), 9057–9063. https://doi.org/10.1002/2015GL066268

Madeleine, J. B., Forget, F., Millour, E., Navarro, T., & Spiga, A. (2012). The influence of radiatively active water ice clouds on the Martian climate. *Geophysical Research Letters*, *39*(23), L23202. https://doi.org/10.1029/2012GL053564

McCleese, D. J. (2008). MRO Mars climate sounder derived data records v1.0 [Dataset]. NASA Planetary Data System. https://doi.org/10.17189/P73K-XY37

McCleese, D. J., Schofield, J. T., Taylor, F. W., Calcutt, S. B., Foote, M. C., Kass, D. M., et al. (2007). Mars climate sounder: An investigation of thermal and water vapor structure, dust and condensate distributions in the atmosphere, and energy balance of the Polar Regions. *Journal of Geophysical Research*, *112*(E5), E05S06. https://doi.org/10.1029/2006JE002790

McLandress, C. (2002). The seasonal variation of the propagating diurnal tide in the mesosphere and lower thermosphere. Part II: The role of tidal heating and zonal mean winds. *Journal of the Atmospheric Sciences*, *59*(5), 907–922. https://doi.org/10.1175/1520-0469(2002)059<0907:TSVOTP>2.0.CO;2

Montabone, L., Spiga, A., Kass, D. M., Kleinböhl, A., Forget, F., & Millour, E. (2020). Martian year 34 column dust climatology from Mars climate sounder observations: Reconstructed maps and model simulations. *Journal of Geophysical Research: Planets*, *125*(8), e06111. https://doi.org/10.1029/2019JE006111

Navarro, T., Madeleine, J. B., Forget, F., Spiga, A., Millour, E., Montmessin, F., & Määttänen, A. (2014). Global climate modeling of the Martian water cycle with improved microphysics and radiatively active water ice clouds. *Journal of Geophysical Research: Planets*, *119*(7), 1479–1495. https://doi.org/10.1002/2013JE004550

Stcherbinine, A., Vincendon, M., Montmessin, F., Wolff, M. J., Korablev, O., Fedorova, A., et al. (2020). Martian water ice clouds during the 2018 global dust storm as observed by the ACS-MIR channel onboard the trace gas orbiter. *Journal of Geophysical Research: Planets*, *125*(3), e2019JE006300. https://doi.org/10.1029/2019JE006300

Steele, L. J., Kleinböhl, A., Kass, D. M., & Zurek, R. W. (2021). Aerosols and tides in the Martian tropics during southern hemisphere spring equinox from Mars climate sounder data. *Journal of Geophysical Research: Planets*, *126*(4), e06776. https://doi.org/10.1029/2020JE006776

Vlasov, P., Ignatiev, N., Guerlet, S., Grassi, D., Korablev, O., Grigoriev, Đ. Ń., et al. (2022). Martian atmospheric thermal structure and dust distribution during the MY34 global dust storm from ACS TIRVIM nadir observations. *Journal of Geophysical Research: Planets*, *127*(9), e07272. https://doi.org/10.1029/2022JE007272

Wilson, R. J., & Hamilton, K. (1996). Comprehensive model simulation of thermal tides in the Martian atmosphere. *Journal of the Atmospheric Sciences*, *53*(9), 1290–1326. https://doi.org/10.1175/1520-0469(1996)053

Wilson, R. J., Lewis, S. R., & Montabone, L. (2007). Thermal tides in an assimilation of three years of thermal emission spectrometer data from Mars global surveyor. In *LPI editorial board*. In *Seventh international conference on mars* (Vol. 1353, p. 3307).

Wilson, R. J., Millour, E., Navarro, T., Forget, F., & Kahre, M. (2014). GCM simulations of aphelion season tropical cloud and temperature structure. In F. Forget & M. Millour (Eds.), *Mars atmosphere: Modelling and observation, 5th international workshop* (p. 1304).

Wilson, R. J., & Richardson, M. I. (1999). Comparison of Mars GCM dust storm simulations with Viking mission observations. In *The fifth international conference on mars* (p. 6234).

Wilson, R. J., & Richardson, M. I. (2000). The Martian atmosphere during the Viking mission. I. Infrared measurements of atmospheric temperatures revisited. *Icarus*, *145*(2), 555–579. https://doi.org/10.1006/icar.2000.6378

Wu, Z., Li, T., & Dou, X. (2015). Seasonal variation of Martian middle atmosphere tides observed by the Mars Climate Sounder. *Journal of Geophysical Research: Planets*, *120*(12), 2206–2223. https://doi.org/10.1002/2015JE004922

Wu, Z., Li, T., & Dou, X. (2017). What causes seasonal variation of migrating diurnal tide observed by the Mars Climate Sounder? *Journal of Geophysical Research: Planets*, *122*(6), 1227–1242. https://doi.org/10.1002/2017JE005277

Wu, Z., Li, T., Li, J., Zhang, X., Yang, C., & Cui, J. (2021). Abnormal phase structure of thermal tides during major dust storms on Mars: Implications for the excitation source of high altitude water ice clouds. *Journal of Geophysical Research: Planets*, *126*(4), e06758. https://doi.org/10.1029/2020JE006758

Young, R. M. B., Millour, E., Guerlet, S., Forget, F., Ignatiev, N., Grigoriev, A. V., et al. (2022). Assimilation of temperatures and column dust opacities measured by ExoMars TGO-ACS-TIRVIM during the MY34 global dust storm. *Journal of Geophysical Research: Planets*, *127*(9), e07312. https://doi.org/10.1029/2022JE007312

Zurek, R. W. (1976). Diurnal tide in the Martian atmosphere. *Journal of the Atmospheric Sciences*, *33*(2), 321–337. https://doi.org/10.1175/1520-0469(1976)033